IOP Publishing | International Atomic Energy Agency Nuclear Fusion

Nucl. Fusion **55** (2015) 093005 (20pp) doi:10.1088/0029-5515/55/9/093005

Physics-model-based nonlinear actuator trajectory optimization and safety factor profile feedback control for advanced scenario development in DIII-D

J.E. Barton[1], M.D. Boyer[1,2], W. Shi[1], W.P. Wehner[1], E. Schuster[1], J.R. Ferron[3], M.L. Walker[3], D.A. Humphreys[3], T.C. Luce[3], F. Turco[4], B.G. Penaflor[3] and R.D. Johnson[3]

[1] Department of Mechanical Engineering and Mechanics, Lehigh University, 19 Memorial Drive West, Bethlehem, PA 18015, USA
[2] Oak Ridge Institute for Science Education, Oak Ridge, TN 37830, USA
[3] General Atomics, 3550 General Atomics Court, San Diego, CA 92121, USA
[4] Columbia University, New York, NY 10027, USA

E-mail: justin.barton@alum.lehigh.edu

Received 16 January 2015, revised 23 May 2015
Accepted for publication 11 June 2015
Published 30 July 2015

Abstract

DIII-D experimental results are reported to demonstrate the potential of physics-model-based safety factor profile control for robust and reproducible sustainment of advanced scenarios. In the absence of feedback control, variability in wall conditions and plasma impurities, as well as drifts due to external disturbances, can limit the reproducibility of discharges with simple pre-programmed scenario trajectories. The control architecture utilized is a feedforward + feedback scheme where the feedforward commands are computed off-line and the feedback commands are computed on-line. In this work, a first-principles-driven (FPD), physics-based model of the q profile and normalized beta (β_N) dynamics is first embedded into a numerical optimization algorithm to design feedforward actuator trajectories that steer the plasma through the tokamak operating space to reach a desired stationary target state that is characterized by the achieved q profile and β_N. Good agreement between experimental results and simulations demonstrates the accuracy of the models employed for physics-model-based control design. Second, a feedback algorithm for q profile control is designed following an FPD approach, and the ability of the controller to achieve and maintain a target q profile evolution is tested in DIII-D high confinement (H-mode) experiments. The controller is shown to be able to effectively control the q profile when β_N is relatively close to the target, indicating the need for integrated q profile and β_N control to further enhance the ability to achieve robust scenario execution. The ability of an integrated q profile + β_N feedback controller to track a desired target is demonstrated through simulation.

Keywords: plasma control, advanced scenario control, model-based control, safety factor profile control

(Some figures may appear in colour only in the online journal)

1. Introduction

Extensive research has been conducted to find advanced regimes of tokamak operation [1] with the goal of developing candidate operating scenarios for ITER. These scenarios are characterized by a high fusion gain, good plasma confinement, magnetohydrodynamic (MHD) stability and a noninductively driven plasma current with a dominant fraction coming from the

bootstrap current [2] so as to minimize the necessary amount of auxiliary current drive needed to maintain the desired scenario [3]. Additionally, advanced scenarios operate close to operational boundaries in terms of both proximity to stability limits (to maximize plasma performance) and available actuation capabilities. As a result, variations in the plasma evolution due to drifts caused by external plasma disturbances, such as variability in the condition of the tokamak walls, plasma impurities, the plasma response to the actuators and actuator faults, can lead to difficulties with reproducibility of target plasma conditions. Two plasma properties that are often used to define a plasma scenario are the safety factor profile (q profile) and the normalized plasma beta (β_N). Therefore control of the q profile, and its eventual integration with β_N control, have the potential to improve the ability to robustly achieve target plasma scenarios. In this work, experimental results are reported to demonstrate the q profile control capabilities in DIII-D.

The q profile is a key plasma property investigated in the development of advanced scenarios due to the close relationship the q profile has with plasma transport [4, 5] (affects bootstrap current drive, auxiliary current drive, and fusion gain) and stability limits that are approached by increasing the plasma pressure [6, 7]. Due to this complex set of interactions, as well as variability in the plasma response, impurities, and drifts due to external disturbances, the problems of predicting and experimentally achieving advanced scenarios are extremely challenging. This motivates the design of feedforward + feedback controllers, which are derived by embedding the known physics of the plasma (described by relevant models) into the design process through *model-based* design techniques, to regulate plasma conditions. As a result of the embedded physics, model-based controllers know in which direction to actuate to generate a desired plasma response and can be designed to share the available actuation capabilities. The ability to robustly achieve and maintain target plasma states through feedback can enable the study of desired regimes, control the proximity to stability limits, and maximize the physics output of the executed discharges. The reported results show the potential of physics-model-based controllers to meet these demanding challenges.

The development of advanced scenarios is experimentally explored by specifying the device's actuator trajectory waveforms, such as the total plasma current and auxiliary heating and current-drive (H&CD) scheme, and analyzing the resulting plasma state evolution. This is conventionally referred to as advanced plasma scenario planning. Traditionally, these feedforward actuator trajectories are developed through a substantial number of trial-and-error attempts and based on extensive experience gained during operation of a particular device. In this work, a model of the plasma dynamics is embedded into a numerical optimization algorithm to synthesize feedforward trajectories for the tokamak actuators that steer the plasma through the tokamak operating space to a predefined target scenario. In this way, actuator trajectories can be designed by exploiting the accumulated knowledge gained by the plasma physics community regarding both the multivariable, coupled, nonlinear, distributed plasma dynamics and plasma stability limits. The numerical optimization algorithm is designed to complement the experimental effort of, and to develop a systematic approach to, advanced scenario planning in the DIII-D tokamak. Ideally, one would like to embed complex simulation codes, such as TRANSP [8], ONETWO [9], and CORSICA [10], into the numerical optimization algorithm. However, as these codes contain highly sophisticated models of the plasma dynamics, they require a substantial amount of computational time to simulate a plasma discharge. As many state-of-the-art optimization algorithms use an iterative approach to find the optimal solution to a problem [11], a more computationally efficient model of the plasma dynamics is needed in practice. The alternative type of model we propose to use is obtained by employing a method that we refer to as a first-principles-driven (FPD), physics-based modeling approach.

The foundation of FPD models is the fundamental physical laws that govern the evolution of the plasma, such as the poloidal magnetic flux diffusion equation. The goal in the development of FPD physics-based models of the plasma dynamics is the conversion of these accepted physics models into a form suitable for control design. Where first-principles knowledge of a particular plasma parameter is either too complex for control design or not fully understood, e.g. the plasma thermal conductivity, general physical observations, which are not unique to any one machine, and experimental/simulated data are used to close the first-principles model by developing a simplified model of the plasma parameter in question, thereby obtaining a *first-principles-driven, physics-based* model. As these models mainly rely on fundamental physical laws, they can readily be adapted to a given operating scenario (characterized by a specified magnetic configuration, heating/current-drive scheme, etc) in a given machine of interest. Progress towards physics-based, control-oriented modeling of the magnetic and kinetic plasma profile evolutions has been recently reported in [12–14]. Models of this complexity can be utilized to simulate a tokamak discharge with a computational time on the order of seconds, and therefore are ideal candidates for the models that can be embedded in an iterative optimization algorithm [11]. Advances in actuator trajectory optimization in low confinement (L-mode) scenarios at the DIII-D and TCV tokamaks that employ physics-based models of the plasma dynamics can be found in [15–17].

To improve the ability to robustly achieve plasma target conditions and compensate for external disturbances and actuation limitations (either in regulation (saturation and rate limits) or due to faults), the feedforward trajectories are integrated together with a feedback control scheme. Feedback control schemes can be developed by employing data-driven or FPD, physics-based techniques. Advances in developing models/profile control strategies following a data-driven approach are discussed in [18–25]. Advances in developing profile control strategies following FPD techniques are discussed in [26–35]. In this work, we follow an FPD approach to design feedback algorithms, as FPD models provide the freedom to handle the trade-off between the physics accuracy and the tractability for control design of the models. Experiments at DIII-D [36–39] represent the first successful demonstration of FPD closed-loop q profile control (in L-mode scenarios) in a tokamak device. In this work, the control philosophy employed in [36–39] is

extended to high confinement (H-mode) scenarios in DIII-D to actively control the q profile through feedback. The developed feedback scheme can be designed to more heavily weight particular regions of interest of the q profile relative to others, and therefore can be readily tailored to suit the needs of various physics experiments. The total plasma current and the auxiliary H&CD system are used as actuators by the feedback controller. The auxiliary H&CD actuators on DIII-D considered in this work are six electron cyclotron wave sources (gyrotrons), which are grouped together to form one effective source for feedback control, and six individual co-current neutral beam injection (NBI) sources, which are referred to by the names [30L/R, 150L/R, 330L/R], where L and R denote left and right lines, respectively. In the H&CD scheme considered, the electron cyclotron sources and the 150L/R NBI lines are utilized as off-axis H&CD sources, while the 30L/R and 330L/R NBI lines are utilized as on-axis H&CD sources.

This paper is organized as follows. In section 2, an FPD model of the plasma current profile dynamics is developed. We begin the model development process by considering the well known one-dimensional poloidal magnetic flux diffusion equation [40], which describes the resistive diffusion of the poloidal magnetic flux in the tokamak in response to the electric field due to induction, the noninductive current driven by the auxiliary H&CD system, and the neoclassical bootstrap effect. This physics model is subsequently converted into a form suitable for control design by developing simplified control-oriented versions of physics-based models of the electron density, the electron temperature, the plasma resistivity, and the noninductively driven currents (auxiliary and bootstrap) in response to the control actuators. In section 3, the developed FPD model is embedded into a numerical optimization algorithm to design actuator trajectories that steer the plasma to a stationary plasma state characterized by the q profile and β_N. The optimized trajectories are subsequently tested experimentally in DIII-D. In section 4, a feedback algorithm for q profile control is designed following an FPD approach. The controller is designed to be robust to uncertainties in the electron density, the electron temperature, and the plasma resistivity, which provides confidence that the controller can be used in a variety of operating conditions. The ability of the q profile controller (not including β_N control) to achieve and maintain a desired safety factor profile evolution is tested in DIII-D H-mode experiments in section 5. The controller is shown to be able to effectively control the q profile when β_N is relatively close to the target. Therefore, to further enhance the ability to achieve robust scenario execution, an integrated q profile + β_N feedback controller is designed and tested through simulations based on the developed FPD, physics-based model in section 6. Finally, conclusions are discussed in section 7.

2. Plasma magnetic and thermal state evolution models

In a well confined tokamak plasma, nested surfaces of constant poloidal magnetic flux are obtained and any quantity that is constant on each surface can be used to index them. In this work, the mean effective minor radius, ρ, of the magnetic flux surface, i.e. $\Phi = \pi B_{\phi,0}\rho^2$, is chosen as the variable to index the magnetic flux surfaces, where Φ is the toroidal magnetic flux and $B_{\phi,0}$ is the vacuum toroidal magnetic field at the geometric major radius R_0 of the tokamak. We define the normalized effective minor radius as $\hat{\rho} = \rho/\rho_b$, where ρ_b is the mean effective minor radius of the last closed magnetic flux surface.

The plasma parameters that characterize a tokamak operating scenario considered in this work are the q profile, the plasma β_N and the plasma loop-voltage profile (U_p). The q profile is related to the spatial gradient of the poloidal magnetic flux (Ψ) and is defined as

$$q(\hat{\rho},t) = -\frac{d\Phi}{d\Psi} = -\frac{d\Phi}{2\pi d\psi} = -\frac{B_{\phi,0}\rho_b^2\hat{\rho}}{\partial\psi/\partial\hat{\rho}}, \tag{1}$$

where we have utilized the relationship between the toroidal magnetic flux and the mean effective minor radius of the magnetic flux surface ($\Phi = \pi B_{\phi,0}\rho^2$), t is the time and ψ is the poloidal stream function, which is closely related to the poloidal flux ($\Psi = 2\pi\psi$). The plasma β_N is related to the volume-averaged plasma stored energy E and is defined as

$$\beta_N = \beta_t[\%]\frac{aB_{\phi,0}}{I_p[\mathrm{MA}]} \quad \beta_t = \frac{\langle p\rangle_V}{B_{\phi,0}^2/(2\mu_0)} = \frac{(2/3)(E/V_p)}{B_{\phi,0}^2/(2\mu_0)}, \tag{2}$$

where β_t is the toroidal plasma beta, a is the plasma minor radius, I_p is the total plasma current, p is the plasma kinetic pressure, $\langle\cdot\rangle_V$ denotes the volume-average operation $1/V_p\int_V(\cdot)dV$, V is the volume enclosed by a magnetic flux surface, V_p is the total plasma volume, and μ_0 is the vacuum magnetic permeability, and we have assumed that the plasma electron and ion densities and temperatures, respectively, are equal. The plasma loop-voltage profile is related to the temporal derivative of the poloidal magnetic flux and is defined as

$$U_p(\hat{\rho},t) = -\frac{\partial\Psi}{\partial t} = -2\pi\frac{\partial\psi}{\partial t}. \tag{3}$$

From (1)–(3), we see that the q profile, plasma β_N, and loop-voltage profile are related to the plasma magnetic and thermal states, ψ and E, respectively. Therefore, we begin by developing physics-based control-oriented models for the evolution of ψ and E, and hence q, β_N, and U_p, respectively.

Under the simplifying assumption of a fixed magnetic geometry (both the plasma boundary as well as the topology of the internal magnetic flux surfaces), the evolution of the poloidal magnetic flux is given in normalized cylindrical coordinates by the magnetic diffusion equation [40]

$$\frac{\partial\psi}{\partial t} = \frac{\eta(T_e,Z_{eff})}{\mu_0\rho_b^2\hat{F}^2}\frac{1}{\hat{\rho}}\frac{\partial}{\partial\hat{\rho}}\left(\hat{\rho}\hat{F}\hat{G}\hat{H}\frac{\partial\psi}{\partial\hat{\rho}}\right) + R_0\hat{H}\eta(T_e,Z_{eff})\frac{\langle\bar{j}_{ni}\cdot\bar{B}\rangle}{B_{\phi,0}}, \tag{4}$$

with boundary conditions given by

$$\left.\frac{\partial\psi}{\partial\hat{\rho}}\right|_{\hat{\rho}=0} = 0 \qquad \left.\frac{\partial\psi}{\partial\hat{\rho}}\right|_{\hat{\rho}=1} = -\frac{\mu_0}{2\pi}\frac{R_0}{\hat{G}(1)\hat{H}(1)}I_p(t), \tag{5}$$

where η is the plasma resistivity, T_e is the electron temperature, Z_{eff} is the effective average charge of the ions in the plasma, $\bar{j}_{ni}$ is any source of noninductive current density (electron cyclotron heating/current drive, neutral beam heating/current drive, bootstrap current drive, etc), $\bar{B}$ is the magnetic field, and $\langle\rangle$ denotes a flux-surface average. The parameters $\hat{F}$, $\hat{G}$, and $\hat{H}$ are geometric factors pertaining to the configuration of the fixed magnetic geometry and are shown in figure 1(*a*). These parameters are defined as

$$\hat{F}(\hat{\rho}) = \frac{R_0 B_{\phi,0}}{R B_\phi(R,Z)} \qquad \hat{G}(\hat{\rho}) = \left\langle \frac{R_0^2}{R^2}|\nabla\rho|^2 \right\rangle$$

$$\hat{H}(\hat{\rho}) = \frac{\hat{F}}{\langle R_0^2/R^2\rangle},$$

where B_ϕ is the toroidal magnetic field at the spatial location (R, Z) in the poloidal plane of the tokamak. Additionally, under the fixed magnetic geometry assumption, an approximate 0D (zero-dimensional) plasma energy balance equation is given by the ordinary differential equation

$$\begin{aligned}\frac{dE}{dt} &= -P_{loss} + P_{ohm} + P_{aux} - P_{rad},\\ &= -\frac{E}{\tau_E} + P_{tot},\end{aligned} \tag{6}$$

where $P_{loss} = E/\tau_E$ is the total power crossing the plasma boundary, τ_E is the global energy confinement time, P_{ohm} is the ohmic power, P_{aux} is the total auxiliary H&CD power, P_{rad} is the radiated power, and $P_{tot} = P_{ohm} + P_{aux} - P_{rad}$ is the total power injected into the plasma. The energy confinement scaling used in this work is the IPB98(y,2) scaling law [41].

To close the dynamic plasma state model (4)–(6), we develop simplified, physics-based models for the evolution of the electron density, the electron temperature, the plasma resistivity, and the noninductive current sources (both auxiliary and bootstrap). The objective in developing the simplified physics-based models of the plasma parameters is to capture the dominant physics that describe how the control actuators (the total plasma current, which is itself controlled by the poloidal field coil system, auxiliary heating/current-drive sources, which are comprised of electron cyclotron and neutral beam launchers on DIII-D, and electron density) affect the plasma parameters, and hence the q profile evolution.

2.1. Electron density modeling

The electron density evolution $n_e(\hat{\rho}, t)$ is modeled as

$$n_e(\hat{\rho}, t) = n_e^{prof}(\hat{\rho})\bar{n}_e(t), \tag{7}$$

where $n_e^{prof}(\hat{\rho})$ is a reference electron density profile, which is shown in figure 1(*c*), and $\bar{n}_e$ is the line average electron density. This model assumes that the control action employed to regulate the electron density weakly affects the radial distribution of the electrons. This is equivalent to assuming that transport, and not the particle sources, determines the shape of the profile. Note that n_e^{prof} is obtained by evaluating the experimental n_e at a reference time $t_{r_{ne}}$, i.e. $n_e^{prof}(\hat{\rho}) = n_e(\hat{\rho}, t_{r_{ne}})/\bar{n}_e(t_{r_{ne}})$.

2.2. Electron temperature modeling

The characteristic thermal diffusion time in the plasma is much faster than the characteristic resistive diffusion time; therefore, the temperature is always in quasi-equilibrium on the time-scale of the current evolution. As a result, we neglect the temporal dynamics of the electron temperature in the development of the electron temperature evolution model, as we are mainly concerned with capturing the dominant physical effects that the electron temperature has on the plasma magnetic profile evolution. Under this condition, from (6), we obtain

$$\frac{3k_{J\,keV}\langle n_e\rangle_V\langle T_e\rangle_V V_p}{\tau_E} = P_{tot}, \tag{8}$$

where we have assumed, as an approximation, equal electron and ion temperatures and densities, i.e. $T_e(\hat{\rho}, t) = T_i(\hat{\rho}, t)$ and $n_e(\hat{\rho}, t) = n_i(\hat{\rho}, t)$, where $T_i(\hat{\rho}, t)$ and $n_i(\hat{\rho}, t)$ are the ion temperature and density profiles, respectively, $k_{J\,keV} = e \times 1V \times 1000$ and e is the elementary charge. Various energy confinement scaling laws have been developed over the years to fit experimentally observed plasma behavior, such as the IPB98(y,2) [41] and Goldston scaling laws [42]. Typically, these scaling laws are functions of the actuators utilized for plasma control, i.e. $\tau_E \propto I_p^{\gamma_s} P_{tot}^{\varepsilon_s} n_e^{\zeta_s}$, where γ_s, ε_s and ζ_s depend on the scaling law utilized. If, as with the IPB98(y,2) and Goldston scaling laws, τ_E is not an explicit function of the temperature, we obtain

$$\langle T_e\rangle_V \propto I_p^{\gamma_s} P_{tot}^{(1+\varepsilon_s)} \langle n_e\rangle_V^{(\zeta_s - 1)}, \tag{9}$$

from (8). Utilizing this result, and based on the TRANSP [8] analyzed electron temperature profile evolution exhibiting a similar behavior across the entire spatial domain (both inside and outside the edge transport barrier) in the considered H-mode scenarios, we model the slowly evolving (on the resistive current diffusion time-scale) electron temperature evolution $T_e(\hat{\rho}, t)$ as a static map of the control actuators, which is expressed as

$$T_e(\hat{\rho}, t) = k_{T_e}(\hat{\rho}) T_e^{prof}(\hat{\rho}) I_p(t) P_{tot}(t)^{1/2} n_e(\hat{\rho}, t)^{-1}, \tag{10}$$

where k_{T_e} is a normalizing profile and $T_e^{prof}(\hat{\rho})$ is a reference profile, which is shown in figure 1(*d*). To arrive at the model shown in (10), the constants in (9) are chosen according to the Goldston scaling law as $\gamma_s = 1$, $\varepsilon_s = -0.5$ and $\xi_s = 0$. Note that T_e^{prof} is obtained by evaluating the experimental T_e at a reference time $t_{r_{Te}}$, i.e. $T_e^{prof}(\hat{\rho}) = T_e(\hat{\rho}, t_{r_{Te}})$. The constant k_{T_e} is also evaluated at a reference time $t_{r_{Te}}$, which is shown in figure 1(*e*), and is expressed as

$$k_{T_e}(\hat{\rho}) = [I_p(t_{r_{Te}}) P_{tot}(t_{r_{Te}})^{1/2} n_e(\hat{\rho}, t_{r_{Te}})^{-1}\,\mathrm{A\,W^{1/2}\,m^{(-3)^{-1}}}]^{-1}.$$

The model (10) qualitatively describes the slowly evolving electron temperature in response to the control actuators, i.e. the observation of (i) an increase in plasma confinement, and hence an increase in temperature, with increasing plasma current, and (ii) a decrease in plasma confinement with increasing total injected power [42]. Also, by changing the electron density, the electron temperature is modified for a given electron pressure.

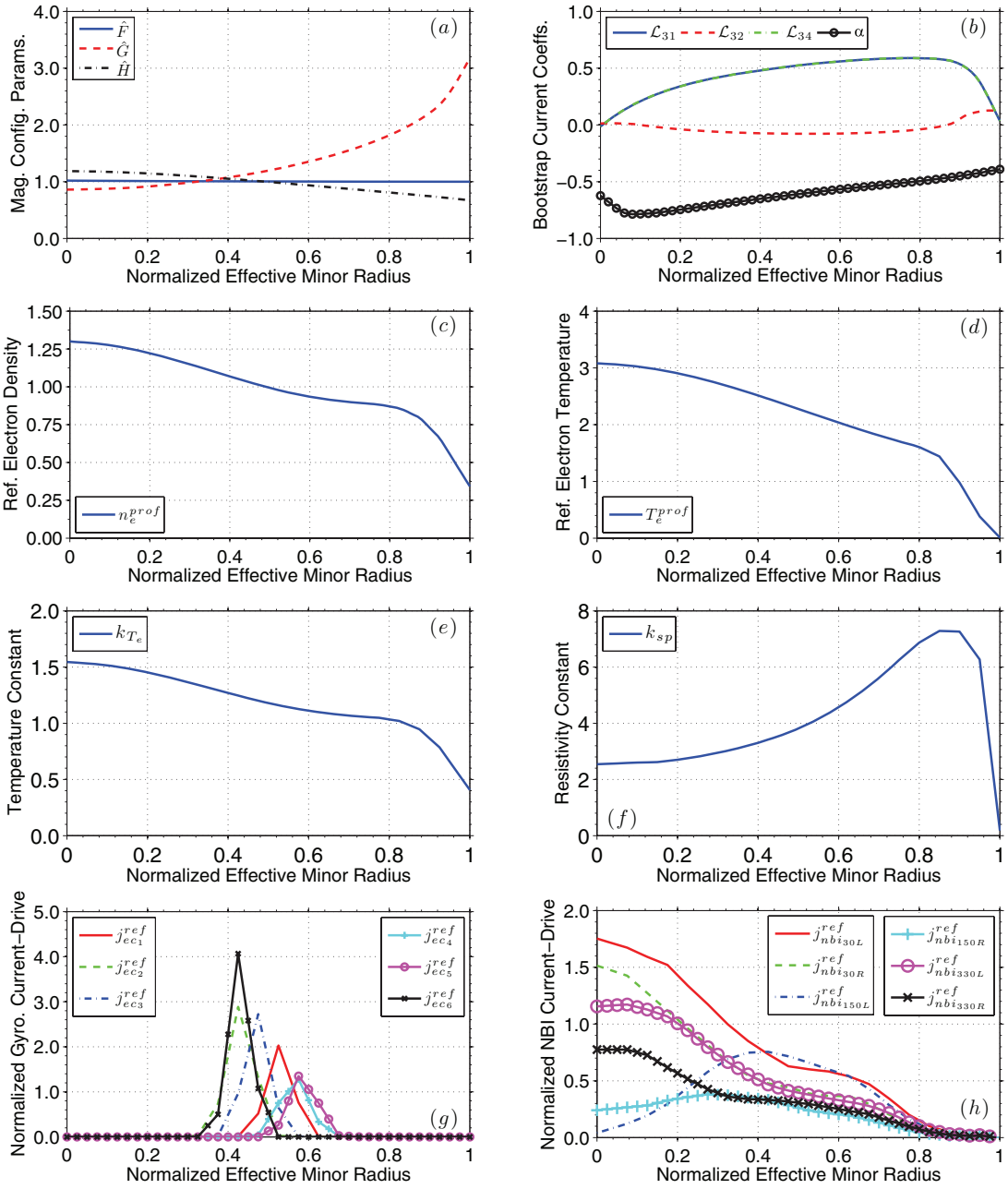

Figure 1. Model parameters tailored to DIII-D tokamak: (*a*) magnetic equilibrium configuration parameters $\hat{F}(\hat{\rho})$, $\hat{G}(\hat{\rho})$, and $\hat{H}(\hat{\rho})$, (*b*) bootstrap current coefficients $\mathcal{L}_{31}(\hat{\rho})$, $\mathcal{L}_{32}(\hat{\rho})$, $\mathcal{L}_{34}(\hat{\rho})$, and $\alpha(\hat{\rho})$, (*c*) reference electron density profile $n_e^{\text{prof}}(\hat{\rho})$, (*d*) reference electron temperature profile $T_e^{\text{prof}}(\hat{\rho})$ (keV), (*e*) electron temperature coefficient k_{T_e} (10^{10} m^{-3} A^{-1} W$^{-1/2}$), (*f*) plasma resistivity coefficient k_{sp} (10^{-8} Ω m keV$^{3/2}$), (*g*) normalized electron cyclotron ($j_{\text{ec}_i}^{\text{ref}}(\hat{\rho})$), for $i \in [1, 2, 3, 4, 5, 6]$, current-drive reference profiles (10^{18} m^{-3} keV^{-1} W^{-1} A m^{-2}), and (*h*) normalized neutral beam ($j_{\text{nbi}_i}^{\text{ref}}(\hat{\rho})$), for $i \in$ [30L/R, 150L/R, 330L/R], current-drive reference profiles (10^{18} m^{-3} keV$^{-1/2}$ W^{-1} A m^{-2}).

The total power injected into the plasma is comprised of the ohmic power, the auxiliary H&CD power and the radiated power. The ohmic power is modeled as

$$P_{\text{ohm}}(t) = \int_0^1 j_{\text{tor}}(\hat{\rho}, t)^2 \eta(\hat{\rho}, t) \frac{\mathrm{d}V}{\mathrm{d}\hat{\rho}} \mathrm{d}\hat{\rho} \approx \mathcal{R}_{\text{p}}(t) I_{\text{p}}(t)^2,$$

where $j_{\text{tor}}(\hat{\rho}, t)$ is the total toroidal current density and $\mathcal{R}_{\text{p}}(t)$ is the global plasma resistance, which is expressed as

$$\mathcal{R}_p(t) \approx 2\pi R_0 \Big/ \int_0^1 \left[\frac{1}{\eta(\hat{\rho}, t)} \frac{\mathrm{d}S}{\mathrm{d}\hat{\rho}} \mathrm{d}\hat{\rho} \right],$$

where S denotes the poloidal cross sectional area enclosed by a magnetic surface within the plasma. The total auxiliary H&CD power is expressed as

$$P_{\text{aux}}(t) = \sum_{i=1}^{n_{\text{ec}}} P_{\text{ec}_i}(t) + \sum_{i=1}^{n_{\text{nbi}}} P_{\text{nbi}_i}(t),$$

where $P_{\text{ec}_i}(t)$ are the individual gyrotron launcher powers, $P_{\text{nbi}_i}(t)$ are the individual neutral beam injector powers and n_{ec} and n_{nbi} are the total numbers of gyrotron and neutral beam launchers, respectively. The radiative power losses considered

in this work are due to Bremsstrahlung radiation, which is modeled as

$$Q_{\rm rad}(\hat{\rho},t) = k_{\rm brem} Z_{\rm eff} n_{\rm e}(\hat{\rho},t)^2 \sqrt{T_{\rm e}(\hat{\rho},t)},$$

where $k_{\rm brem} = 5.5\times10^{-37}\,{\rm W\,m^3}\sqrt{\rm keV}^{-1}$ is the Bremsstrahlung radiation coefficient. Other sources of radiation losses, such as line or cyclotron radiation losses, could be incorporated into the model as needed depending on the studied scenarios. The radiated power is then expressed as

$$P_{\rm rad}(t) = \int_0^1 Q_{\rm rad}(\hat{\rho},t)\frac{{\rm d}V}{{\rm d}\hat{\rho}}{\rm d}\hat{\rho}.$$

2.3. Plasma resistivity modeling

The resistivity η scales with the electron temperature and is modeled by utilizing a simplified Spitzer resistivity model as

$$\eta(\hat{\rho},t) = k_{\rm sp}(\hat{\rho}) Z_{\rm eff} / [T_{\rm e}(\hat{\rho},t)^{3/2}], \tag{11}$$

where $k_{\rm sp}(\hat{\rho}) = [\eta(\hat{\rho},t_{\rm r_\eta})T_{\rm e}(\hat{\rho},t_{\rm r_\eta})^{3/2}]/Z_{\rm eff}\,\Omega\,{\rm m\,(keV)^{3/2}}$ is a profile that is evaluated at a reference time $t_{\rm r_\eta}$ and is shown in figure 1(*f*). We neglect neoclassical corrections to this formula to retain the dominant temperature dependence. In this work, we assume $Z_{\rm eff}$ to be constant in both space and time. In reality, $Z_{\rm eff}$ varies in both space and time due to particle recycling, particle sputtering from the plasma facing components, plasma fueling, controlled impurity injection and particle diffusion in the plasma. In the developed modeling framework, a spatial variation of $Z_{\rm eff}$ could be incorporated in a straightforward manner, i.e. $Z_{\rm eff} = Z_{\rm eff}(\hat{\rho})$. Incorporating a temporal variation of $Z_{\rm eff}$ would require additional modeling work to capture the effects that the previously mentioned physical mechanisms have on the particle density evolution in the plasma.

2.4. Noninductive current-drive modeling

The noninductively driven current is expressed as

$$\frac{\langle \bar{j}_{\rm ni}\cdot\bar{B}\rangle}{B_{\phi,0}} = \sum_{i=1}^{n_{\rm ec}}\frac{\langle \bar{j}_{{\rm ec}_i}\cdot\bar{B}\rangle}{B_{\phi,0}} + \sum_{i=1}^{n_{\rm nbi}}\frac{\langle \bar{j}_{{\rm nbi}_i}\cdot\bar{B}\rangle}{B_{\phi,0}} + \frac{\langle \bar{j}_{\rm bs}\cdot\bar{B}\rangle}{B_{\phi,0}}, \tag{12}$$

where $\bar{j}_{{\rm ec}_i}$ is the noninductive current generated by the individual gyrotron launchers, $\bar{j}_{{\rm nbi}_i}$ is the noninductive current generated by the individual neutral beam injectors, and $\bar{j}_{\rm bs}$ is the noninductive current generated by the bootstrap effect.

2.4.1. Auxiliary current-drive modeling. We model each auxiliary noninductive current source as the time varying power in each actuator multiplied by a constant deposition profile in space, i.e.

$$\frac{\langle \bar{j}_i\cdot\bar{B}\rangle}{B_{\phi,0}}(\hat{\rho},t) = k_i(\hat{\rho}) j_i^{\rm dep}(\hat{\rho})\frac{T_{\rm e}(\hat{\rho},t)^\delta}{n_{\rm e}(\hat{\rho},t)}P_i(t) = j_i^{\rm ref}(\hat{\rho})\frac{T_{\rm e}(\hat{\rho},t)^\delta}{n_{\rm e}(\hat{\rho},t)}P_i(t), \tag{13}$$

where $i\in[{\rm ec}_1,\ldots,{\rm ec}_{n_{\rm ec}},{\rm nbi}_1,\ldots,{\rm nbi}_{n_{\rm nbi}}]$, k_i is a normalizing profile, $j_i^{\rm dep}(\hat{\rho})$ is a current density deposition profile for each auxiliary source, the term $T_{\rm e}^\delta/n_{\rm e}$ represents the current-drive efficiency and $j_i^{\rm ref} = k_i j_i^{\rm dep}$. For electron cyclotron current drive $\delta = 1$ [43], and for neutral beam current drive δ is dependent on the energy of the injected particles [44]. The energy of the injected neutral particles on DIII-D is 80 keV; therefore, $\delta = 1/2$ for neutral beam current drive. Note that $j_i^{\rm dep}$ is evaluated at a reference time $t_{\rm r_{aux}}$, i.e. $j_i^{\rm dep}(\hat{\rho}) = [\langle \bar{j}_i\cdot\bar{B}\rangle/B_{\phi,0}](\hat{\rho},t_{\rm r_{aux}})$. The constants k_i are expressed as $k_i(\hat{\rho}) = n_{\rm e}(\hat{\rho},t_{\rm r_{aux}})/[T_{\rm e}(\hat{\rho},t_{\rm r_{aux}})^\delta P_i(t_{\rm r_{aux}})]{\rm m^{-3}/[keV^\delta W]}$ and are also evaluated at a reference time $t_{\rm r_{aux}}$. The normalized electron cyclotron and neutral beam current drive reference profiles are shown in figures 1(*g*) and (*h*).

2.4.2. Bootstrap current-drive modeling. The bootstrap current arises from the inhomogeneity of the magnetic field strength produced by the external coils in the tokamak, which falls off as $1/R$, and is associated with trapped particles. From [45, 46], we write the bootstrap current as

$$\frac{\langle \bar{j}_{\rm bs}\cdot\bar{B}\rangle}{B_{\phi,0}}(\hat{\rho},t) = \frac{k_{\rm J\,keV}R_0}{\hat{F}}\left(\frac{\partial\psi}{\partial\hat{\rho}}\right)^{-1}\left[2\mathcal{L}_{31}T_{\rm e}\frac{\partial n_{\rm e}}{\partial\hat{\rho}} + \{2\mathcal{L}_{31}+\mathcal{L}_{32}+\alpha\mathcal{L}_{34}\}n_{\rm e}\frac{\partial T_{\rm e}}{\partial\hat{\rho}}\right], \tag{14}$$

where $\mathcal{L}_{31}(\hat{\rho})$, $\mathcal{L}_{32}(\hat{\rho})$, $\mathcal{L}_{34}(\hat{\rho})$ and $\alpha(\hat{\rho})$ depend on the magnetic configuration of a particular plasma equilibrium and are shown in figure 1(*b*).

2.5. Physics-based control-oriented model of plasma current profile dynamics

By combining the physics-based models of the electron density (7), electron temperature (10), plasma resistivity (11) and noninductive current-drive models (12)–(14) with the magnetic diffusion equation model (4)–(5), we obtain our desired *first-principles-driven*, physics-based, control-oriented model of the poloidal magnetic flux profile evolution. The nonlinear, physics-based partial differential equation (PDE) model of the poloidal flux evolution is expressed as

$$\frac{\partial\psi}{\partial t} = f_\eta(\hat{\rho})u_\eta(t)\frac{1}{\hat{\rho}}\frac{\partial}{\partial\hat{\rho}}\left(\hat{\rho}D_\psi(\hat{\rho})\frac{\partial\psi}{\partial\hat{\rho}}\right) + \sum_{i=1}^{n_{\rm ec}} f_{{\rm ec}_i}(\hat{\rho})u_{{\rm ec}_i}(t) + \sum_{i=1}^{n_{\rm nbi}} f_{{\rm nbi}_i}(\hat{\rho})u_{{\rm nbi}_i}(t) + f_{\rm bs}(\hat{\rho})u_{\rm bs}(t)\left(\frac{\partial\psi}{\partial\hat{\rho}}\right)^{-1}, \tag{15}$$

with boundary conditions

$$\left.\frac{\partial\psi}{\partial\hat{\rho}}\right|_{\hat{\rho}=0} = 0 \qquad \left.\frac{\partial\psi}{\partial\hat{\rho}}\right|_{\hat{\rho}=1} = -k_{I_{\rm p}}u_{I_{\rm p}}(t), \tag{16}$$

where f_η, $f_{{\rm ec}_i}$, $f_{{\rm nbi}_i}$ and $f_{\rm bs}$ are functions of space, $D_\psi = \hat{F}\hat{G}\hat{H}$ and $k_{I_{\rm p}} = [\mu_0 R_0]/[2\pi\hat{G}(1)\hat{H}(1)]$. The diffusivity ($u_\eta$), interior ($u_{{\rm ec}_i}$, $u_{{\rm nbi}_i}$, $u_{\rm bs}$) and boundary ($u_{I_{\rm p}}$) control terms are expressed as

$$
\begin{aligned}
u_{\eta}(t) &= [I_{\mathrm{p}}(t)P_{\mathrm{tot}}(t)^{1/2}\bar{n}_{\mathrm{e}}(t)^{-1}]^{-3/2},\\
u_{\mathrm{ec}_i}(t) &= [I_{\mathrm{p}}(t)P_{\mathrm{tot}}(t)^{1/2}\bar{n}_{\mathrm{e}}(t)^{-1}]^{-1/2}\bar{n}_{\mathrm{e}}(t)^{-1}P_{\mathrm{ec}_i}(t),\\
u_{\mathrm{nbi}_i}(t) &= [I_{\mathrm{p}}(t)P_{\mathrm{tot}}(t)^{1/2}\bar{n}_{\mathrm{e}}(t)^{-1}]^{-1}\bar{n}_{\mathrm{e}}(t)^{-1}P_{\mathrm{nbi}_i}(t),\\
u_{\mathrm{bs}}(t) &= [I_{\mathrm{p}}(t)P_{\mathrm{tot}}(t)^{1/2}\bar{n}_{\mathrm{e}}(t)^{-1}]^{-1/2}\bar{n}_{\mathrm{e}}(t),\\
u_{I_{\mathrm{p}}}(t) &= I_{\mathrm{p}}(t).
\end{aligned}
\tag{17}
$$

The physics information contained in the nonlinear model is embedded into the feedforward and feedback components of the control scheme through advanced model-based control design techniques.

3. Scenario planning by feedforward actuator trajectory optimization

3.1. Formulation of actuator trajectory optimization problem

The objective of the actuator trajectory optimization algorithm is to design actuator waveforms that steer the plasma from a particular initial condition through the tokamak operating space to reach a target state at some time t_{f} during the discharge. One of the key physics goals of plasma profile control is to reach a target plasma state at a desired time and maintain this state to enable the study of desired regimes and make the best use of the discharge.

3.1.1. Target plasma state: cost functional definition. The target plasma state is chosen to be defined in terms of the q profile and the plasma β_{N}. The goal of the actuator trajectory optimization problem is therefore to reach a target q profile ($q^{\mathrm{tar}}(\hat{\rho})$) and normalized plasma beta ($\beta_{\mathrm{N}}^{\mathrm{tar}}$) at a time t_{f} during the discharge in such a way that the achieved plasma state is as stationary in time as possible. As the poloidal flux profile evolves with the slowest time constant in the plasma, if it reaches a stationary condition, i.e. $U_{\mathrm{p}}(\hat{\rho},t)=$ constant, all of the other plasma profiles have also reached a stationary condition. Therefore, the stationarity of the plasma state can be defined by the profile

$$
g_{\mathrm{ss}}(\hat{\rho},t)=\frac{\partial U_{\mathrm{p}}}{\partial\hat{\rho}}.
$$

A stationary plasma state is reached when $g_{\mathrm{ss}}(\hat{\rho},t)=0$. The proximity of the achieved plasma state to the target state at the time t_{f} can be described by the cost functional

$$
J(t_{\mathrm{f}})=k_{\mathrm{ss}}J_{\mathrm{ss}}(t_{\mathrm{f}})+k_qJ_q(t_{\mathrm{f}})+k_{\beta_{\mathrm{N}}}J_{\beta_{\mathrm{N}}}(t_{\mathrm{f}}),
\tag{18}
$$

where k_{ss}, k_q and $k_{\beta_{\mathrm{N}}}$ are used to weight which characteristics of the plasma state are more important than the others and

$$
J_q(t_{\mathrm{f}})=\int_0^1 W_q(\hat{\rho})[q^{\mathrm{tar}}(\hat{\rho})-q(\hat{\rho},t_{\mathrm{f}})]^2\mathrm{d}\hat{\rho},
\tag{19}
$$

$$
J_{\mathrm{ss}}(t_{\mathrm{f}})=\int_0^1 W_{\mathrm{ss}}(\hat{\rho})[g_{\mathrm{ss}}(\hat{\rho},t_{\mathrm{f}})]^2\mathrm{d}\hat{\rho},
\tag{20}
$$

$$
J_{\beta_{\mathrm{N}}}(t_{\mathrm{f}})=[\beta_{\mathrm{N}}^{\mathrm{tar}}-\beta_{\mathrm{N}}(t_{\mathrm{f}})]^2,
\tag{21}
$$

where $W_q(\hat{\rho})$ and $W_{\mathrm{ss}}(\hat{\rho})$ are functions used to weight which portions of the respective profiles are more important than the others.

3.1.2. Plasma state dynamics: model reduction via spatial discretization. To simulate the physics-based control-oriented model, we spatially discretize the infinite dimensional PDE (15)–(16) by employing a finite difference method, where the nondimensional spatial domain of interest ($\hat{\rho}\in[0,1]$) is represented by m_ψ discrete nodes. After spatially discretizing (15) and taking into account the boundary conditions (16), we obtain a nonlinear finite dimensional ordinary differential equation model defined by

$$
\dot{\hat{\psi}}=f_\psi(\hat{\psi},u),
$$

where $\hat{\psi}=[\psi_2,\psi_3,\ldots,\psi_{m_\psi-1}]^{\mathrm{T}}\in\mathbb{R}^{n_\psi}$ is the plasma magnetic state vector, ψ_i is the value of ψ at the discrete nodes, $u=[P_{\mathrm{ec}_1},\ldots,P_{\mathrm{ec}_{n_{\mathrm{ec}}}},P_{\mathrm{nbi}_1},\ldots,P_{\mathrm{nbi}_{n_{\mathrm{nbi}}}},\bar{n}_{\mathrm{e}},I_{\mathrm{p}}]^{\mathrm{T}}\in\mathbb{R}^{n_{\mathrm{act}}}$ is the control input vector, $n_{\mathrm{act}}=n_{\mathrm{ec}}+n_{\mathrm{nbi}}+2$, $f_\psi\in\mathbb{R}^{n_\psi}$ is a nonlinear function of the plasma magnetic states and control inputs and $n_\psi=m_\psi-2$. By defining the plasma state vector as

$$
x=\begin{bmatrix}\hat{\psi}\\ E\end{bmatrix}\in\mathbb{R}^{n_\psi+1},
$$

we can write the magnetic and kinetic state dynamics as

$$
\dot{x}=\begin{bmatrix}f_\psi(\hat{\psi},u)\\ -\dfrac{E}{\tau_{\mathrm{E}}(t)}+P_{\mathrm{tot}}(x,u)\end{bmatrix}=F_{\psi,E}(x,u)\in\mathbb{R}^{n_\psi+1}.
\tag{22}
$$

We then integrate (22) in time by employing a fully implicit numerical scheme, i.e.

$$
\frac{x_{k+1}-x_k}{\Delta t}=F_{\psi,E}(x_{k+1},u_k),
\tag{23}
$$

where x_k and u_k denote the plasma state and control input, respectively, at the time step t_k, x_{k+1} denotes the plasma state at the next time step t_{k+1} and Δt denotes the simulation time step. The plasma magnetic and thermal state evolution can be obtained by iteratively solving (23) at each simulation time step from a given initial condition $x_0=x(t_0)$, where t_0 is the initial time.

3.1.3. Control actuator trajectory parameterization. The trajectories of the ith control actuator (u_i) are parameterized by a finite number of parameters (n_{p_i}) at discrete points in time (t_{p_i}), i.e. $t_{p_i}=[t_0,t_1,\ldots,t_k,\ldots,t_k=t_{\mathrm{f}}]\in\mathbb{R}^{n_{p_i}}$. During the time interval $t\in(t_k,t_{k+1})$ the ith control input is determined by linear interpolation as $u_i(t)=u_i(t_k)+[u_i(t_{k+1})-u_i(t_k)](t-t_k)/(t_{k+1}-t_k)$. By combining all of the parameters utilized to represent each individual actuator trajectory into a vector

$$
\tilde{\theta}=[u_1^1,\ldots,u_1^{n_{p_1}},\ldots,u_i^1,\ldots,u_i^{n_{p_i}},\ldots,u_{n_{\mathrm{act}}}^1,\ldots,u_{n_{\mathrm{act}}}^{n_{p_{n_{\mathrm{act}}}}}],
\tag{24}
$$

where $\tilde{\theta}\in\mathbb{R}^{n_{\mathrm{p}}^{\mathrm{tot}}}$ and $n_{\mathrm{p}}^{\mathrm{tot}}=\sum_{i=1}^{n_{\mathrm{act}}}n_{p_i}$, the parameterized control actuator trajectories are given by

$$
u(t)=\Pi(t)\tilde{\theta},
\tag{25}
$$

where $\Pi(t) \in \mathbb{R}^{n_{\text{act}} \times n_{\text{p}}^{\text{tot}}}$ is a piecewise linear function of time. Some of the parameters in the vector (24) may be chosen to be fixed due to the desire to obtain an operating condition at the time t_{f} with a specific set of characteristics (a final plasma current ($I_{\text{p}}(t_{\text{f}})$) and/or line average electron density ($\bar{n}_{\text{e}}(t_{\text{f}})$)), or to provide the ability to acquire diagnostic data (constant power in a neutral beam injector). Therefore, the subset of free parameters in the vector (24) can be combined into a vector of to-be-optimized parameters, which we define as $\theta \in \mathbb{R}^{n_{\text{opt}}}$, where $n_{\text{opt}} \leqslant n_{\text{p}}^{\text{tot}}$.

3.1.4. Actuator constraints. The actuator magnitude constraints are defined as

$$I_{\text{p}}^{\min} \leqslant I_{\text{p}}(t) \leqslant I_{\text{p}}^{\max}, \tag{26}$$

$$P_{\text{ec}}^{\min} \leqslant P_{\text{ec}_i}(t) \leqslant P_{\text{ec}}^{\max}, \quad i = 1, \ldots, n_{\text{ec}} \tag{27}$$

$$P_{\text{nbi}}^{\min} \leqslant P_{\text{nbi}_i}(t) \leqslant P_{\text{nbi}}^{\max}, \quad i = 1, \ldots, n_{\text{nbi}} \tag{28}$$

where $(\cdot)^{\min}$ and $(\cdot)^{\max}$ represent the minimum and maximum limits, respectively. Only the total plasma current actuator rate is constrained, and this constraint is given by

$$-I_{p,\max}^{d'} \leqslant \frac{\mathrm{d}I_{\text{p}}}{\mathrm{d}t} \leqslant \Gamma_{p,\max}^{u'} \tag{29}$$

where $I_{p,\max}^{d'}$ and $I_{p,\max}^{u'}$ are the maximum I_{p} ramp-down and ramp-up rates, respectively. The actuator constraints (26)–(29) can be combined together and written in terms of the to-be-optimized parameters θ in a compact matrix form as

$$A_u^{\lim} \theta \leqslant b_u^{\lim}. \tag{30}$$

3.1.5. Plasma state and MHD stability constraints. The MHD stability limit related to the plasma magnetic state considered in this work is expressed as

$$q_{\min}(t) \geqslant q_{\min}^{\lim}, \tag{31}$$

where $q_{\min}(t) = \min\{q(\hat{\rho}, t)\}$ and $q_{\min}^{\lim}$ is a constant chosen to be slightly greater than one to avoid the onset of sawtooth oscillations. In order for the plasma to remain in the H-mode operating regime, the net power across the plasma surface (P_{net}) must be greater than a threshold power ($P_{\text{threshold}}$), i.e.

$$P_{\text{net}}(t) \geqslant P_{\text{threshold}}(t), \tag{32}$$

where

$$P_{\text{net}}(t) = P_{\text{tot}}(t) - \frac{\mathrm{d}E}{\mathrm{d}t} = \frac{E}{\tau_{\text{E}}(t)}$$

and the threshold power is given in [47, 48]. The final MHD stability limit considered in this work is given by

$$\bar{n}_{\text{e}20}(t) \leqslant n_{\text{g}}(t), \tag{33}$$

where $\bar{n}_{\text{e}20}(t)$ is the line average electron density in 10^{20} m^{-3},

$$n_{\text{g}}(t) = \frac{I_{\text{p}}(t)[\text{MA}]}{\pi a^2}$$

is the Greenwald density limit [49] and a is the plasma minor radius. We next chose to formulate the constraints (31)–(32) as integral constraints [50]. This provides us with the ability to reduce the number of constraints imposed on the optimization problem solution. An example of this is given for constraint (31) as

$$c_q^{\lim} = \int_{t_0}^{t_{\text{f}}} \max\{0, q_{\min}^{\lim} - q_{\min}(t)\}\mathrm{d}t \leqslant 0. \tag{34}$$

The plasma state and MHD stability constraint (32) can be written in the form of (34) and combined together and written in a compact matrix form as

$$c_{\text{mhd}}^{\lim}(x(t)) \leqslant 0. \tag{35}$$

As the MHD stability constraint (33) depends directly on the to-be-optimized parameters θ, it is included in the formulation of the actuator constraints (30).

3.1.6. Optimization problem statement and solution method. The nonlinear, constrained, actuator trajectory optimization problem is now to determine the to-be-optimized parameters θ that minimize cost functional (18) subject to the plasma dynamics (22), the control actuator trajectory parameterization (25), the actuator constraints (30), and the plasma state and MHD stability constraints (35). This optimization problem is written mathematically as

$$\min_{\theta} \quad J(t_{\text{f}}) = J(\dot{x}(t_{\text{f}}), x(t_{\text{f}})), \tag{36}$$

such that

$$\begin{aligned} \dot{x} &= F_{\psi,E}(x, u), \\ u(t) &= \Pi(t)\tilde{\theta}, \\ A_u^{\lim}\theta &\leqslant b_u^{\lim}, \\ c_{\text{mhd}}^{\lim}(x(t)) &\leqslant 0. \end{aligned} \tag{37}$$

We solve this optimization problem by employing a method called sequential quadratic programming (SQP) [11]. The SQP solution method is predicated on determining a local minimizer of the nonlinear program (NLP) (36)–(37) by iteratively solving a sequence of quadratic programs (QPs). At each iteration we have a current estimate of a local minimizer of the NLP and a QP which minimizes a quadratic approximation of the original system Hamiltonian subject to a linear approximation of the system constraints around the current estimate. The solution of each QP then yields a step toward the solution of the original NLP. An overview of SQP is provided in appendix A.

3.2. Design and experimental testing of optimized feedforward trajectories

We now solve the actuator trajectory optimization problem (36)–(37) to reach a target plasma state (such that the achieved state is in a stationary condition) at a time t_{f} during the plasma discharge by employing the SQP solution method. The optimization is carried out over the time interval

$t_{opt} = t \in [t_0, t_f] = [0.5, 3.0]$ s. We begin by parameterizing the ith actuator trajectory by $n_{p_i} = 6$ discrete parameters at the time points $t_{p_i} = [0.5, 1.0, \ldots, 3.0]$ s. Next, the components of the total parameter vector (24) that are fixed, or not to be optimized, are chosen as discussed in section 3.1.3. First, the total gyrotron power, $P_{ec_{tot}}(t)$, is chosen to be evenly distributed amongst the individual gyrotron launchers. Additionally, as the gyrotrons have a limited amount of total energy that they can deliver in a plasma discharge, they are set to be inactive during the time interval $t \in [0.5, 2.5)$ s so that they have the potential to be used at full power for the remainder of the discharge. Second, in order to acquire diagnostic data to reconstruct the q profile, the 30L/R neutral beam powers are fixed at a constant 1.1 MW (30L is indeed used for MSE diagnostics but 30R is constrained by phase requirements). Third, density control is challenging in experiments due to large particle recycling at the tokamak wall and to the difficulty of pumping particles out of the machine. Therefore, the line average electron density trajectory is chosen to not be optimized and is specified as follows: linearly ramped up from an initial value of $\bar{n}_e(0.5) = 2 \times 10^{19}$ m^{-3} to a final value of $\bar{n}_e(2.0) = 4.2 \times 10^{19}$ m^{-3} and then held constant. Finally, all of the actuator values at the initial time $t_0 = 0.5$ s and the value of the total plasma current at the time $t_f = 3.0$ s are chosen to be fixed, i.e. they are not optimized. The vector of to-be-optimized parameters is then given by

$$\theta = [P_{ec_{tot}}(2.5), P_{ec_{tot}}(3.0), P_{nbi_i}(1.0), \ldots, P_{nbi_i}(3.0), I_p(1.0), \ldots, I_p(2.5)], \quad (38)$$

where $i \in [150\text{L/R}, 330\text{L/R}]$, respectively. The value and shape of the q profile in the center of the plasma (typically in the spatial domain $\hat{\rho} \in [0, 0.4]$) is important to achieving and maintaining high performance plasmas [4, 5]. As a result, the weight function $W_q(\hat{\rho})$ in (19) is chosen to place more emphasis on achieving the target q profile in the inner region of the plasma ($\hat{\rho} \in [0, 0.4]$) than in the outer region.

The optimized parameters (38) (and associated actuator trajectories) determined by solving the optimization problem (36)–(37), with the target plasma state ($q^{tar}(\hat{\rho})$ and β_N^{tar}) chosen to be the q profile and β_N experimentally achieved at 3.0 s in DIII-D shot 150320, are shown in figure 2. First, the total plasma current is ramped up at the maximum allowable rate, which is set to avoid triggering tearing modes due to a loss of magnetic shear near the plasma boundary, and exhibits a slight overshoot before settling to the specified final value. Second, the off-axis neutral beam power ($P_{nbi_{150L/R}}$) is gradually increased to the maximum allowable value during the time interval $t \in [1.5, 3]$ s to set up a stationary plasma state with off-axis auxiliary current drive, which is needed to achieve the target q profile in the plasma core. Third, the maximum amount of electron cyclotron power is injected into the plasma with the same objective, as well as to reach the target β_N. Finally, a moderate amount of on-axis neutral beam power ($P_{nbi_{330L/R}}$) is injected into the plasma during the time interval $t \in [2, 3]$ s to set up a stationary state before settling to a relatively small value that is needed to achieve the target β_N. As shown in figure 3, the optimized actuator trajectories satisfy the H-mode threshold (32) and density limit (33) constraints that are imposed on the solution of the optimization problem (36)–(37).

The actuator trajectories shown in figure 2 were tested through simulation with the physics-based model of the plasma dynamics (described in section 2) and experimentally in DIII-D during shot 154684. As the optimized trajectories were designed to achieve a target plasma state at the time $t_f = 3.0$ s in such a way that the achieved state is as stationary in time as possible, the actuator values were held constant from the time t_f until the end of the discharge. It is important to note that the optimized trajectories represent the references to the dedicated control loops that command the DIII-D physical actuators, and, as shown in figure 2, the dedicated control loops were able to follow the requested trajectories reasonably well. However, during DIII-D shot 154684, one of the gyrotrons faulted at approximately 3.8 s, the 150R neutral beam injector was saturated at its upper limit after 2.75 s, and the control loop commanding the 150L neutral beam injector was not able to follow the request after 2.5 s.

Time traces of q at various radial locations, a time trace of β_N, and a comparison of the target, physics-based model predicted and experimentally achieved q profiles at various times are shown in figure 4. As shown in the figure, the optimized trajectories were able to drive the experimental plasma as close as possible to the desired stationary q profile at 3.0 s. However, at 2.3 s, MHD instabilities developed and persisted for the remainder of the discharge. The MHD instabilities degraded the plasma confinement characteristics (shown in the immediate reduction of β_N once the modes develop) and resulted in the inability to experimentally achieve the target β_N and maintain the target q profile in the plasma core after 4.0 s. However, through simulation with the physics-based model, it was shown that the optimized trajectories were able to steer the simulated plasma to the stationary target in the absence of MHD modes. Finally, note the good agreement between the simulated (red dashed line) and experimental (black dash–dotted line) q profile evolution during the time interval $t \in [0.5, 4.0]$ s, which provides confidence in the ability of the physics-based model to satisfactorily predict the evolution of the plasma for control algorithm design purposes.

3.3. Discussion and implications of optimized actuator trajectory testing results

As a result of the MHD instabilities that developed during the experimental test of the optimized trajectories, the target β_N was not able to be achieved and the target q profile was unable to be maintained in a stationary condition. Therefore, to compensate for external disturbances (such as a reduction in confinement) and actuation limitations (either in regulation or faults), the feedforward trajectories need to be integrated together with a feedback control scheme, as discussed in the next section, to improve the ability to robustly achieve plasma target conditions.

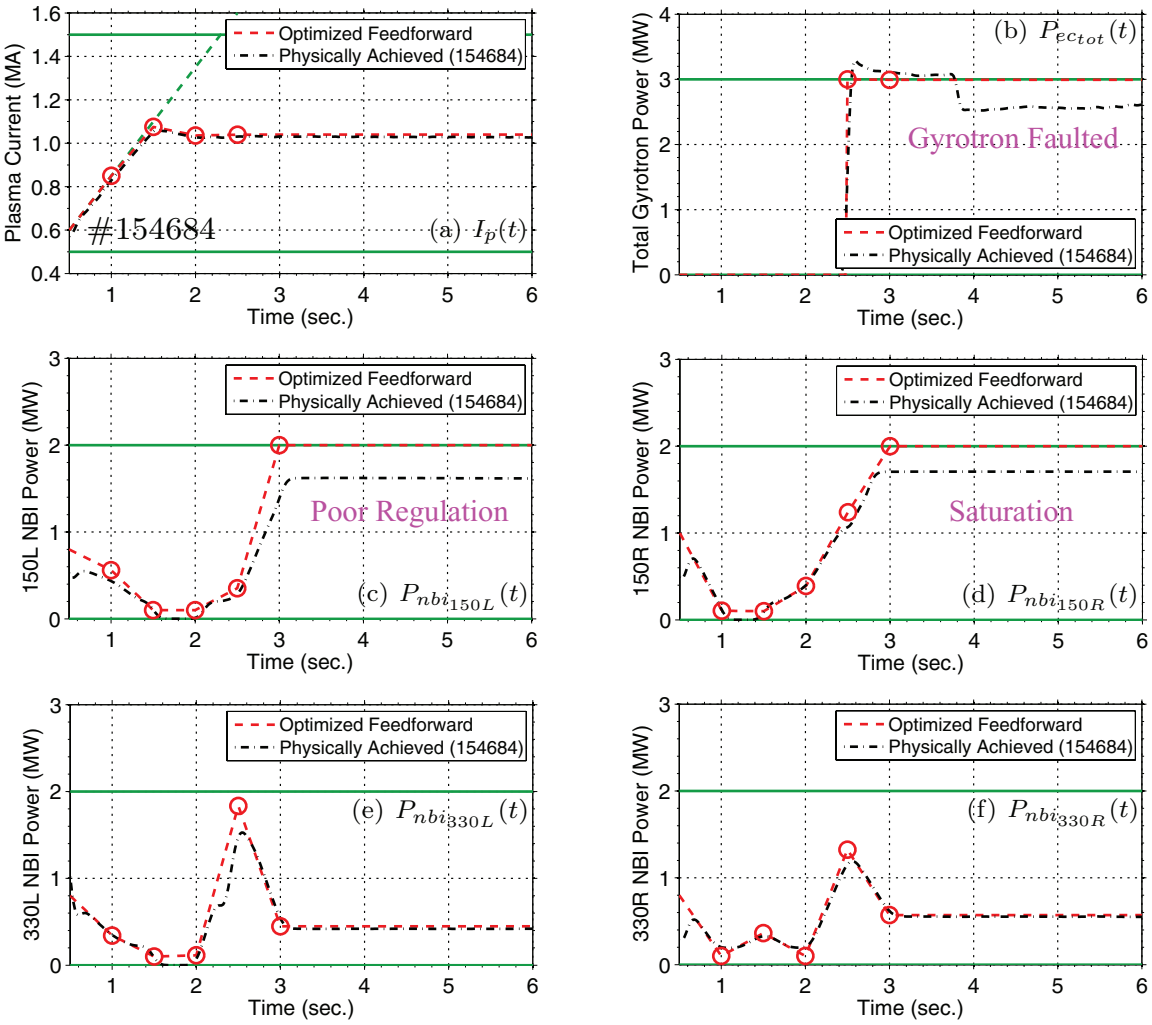

Figure 2. Optimized and physically achieved (DIII-D shot 154684) actuator trajectories: (*a*) total plasma current, (*b*) total electron cyclotron power (set to be inactive during the time interval $t \in [0.5, 2.5)$ s because of the limited amount of total energy that the gyrotrons can deliver in one discharge), and (*c*)–(*f*) individual neutral beam injection powers. Actuator limitations (either in regulation or faults) are indicated in the respective figures. Additionally, the actuator magnitude (solid green) and rate (dashed green) limits applied on the optimization problem solution are also shown. The actuator trajectories are represented by a finite number of parameters (optimized parameter denoted by red circle) and the associated actuator trajectories (red line) are determined by linear interpolation during the time intervals between the individually optimized parameters.

4. Physics-model-based feedback control design

We begin the design process by converting the physics model that describes the poloidal magnetic flux profile evolution in the tokamak (the magnetic diffusion equation (4)) into a form suitable for feedback control design. In this work, we chose to model the kinetic plasma parameters (electron density, electron temperature and plasma resistivity) as a nominal model plus a bounded uncertain model. We then employ *robust control techniques* [52] to design a feedback controller that achieves a desired closed-loop performance while guaranteeing that the controller maintains closed-loop system stability for the range of the kinetic plasma parameters captured by the uncertain models.

Towards this goal, ranges in which the electron density and electron temperature profiles are expected to be in typical DIII-D advanced scenarios are shown in figures 5(*a*) and (*b*). For feedback control design, these plasma parameters are modeled as

$$n_e(\hat{\rho}) = n_e^{nom}(\hat{\rho}) + n_e^{unc}(\hat{\rho})\delta_{n_e}, \tag{39}$$

$$T_e(\hat{\rho}) = T_e^{nom}(\hat{\rho}) + T_e^{unc}(\hat{\rho})\delta_{T_e}, \tag{40}$$

where the nominal (n_e^{nom}, T_e^{nom}) and uncertain (n_e^{unc}, T_e^{unc}) profiles are defined in terms of the maximum and minimum profiles shown in figures 5(*a*) and (*b*) and the uncertain parameters δ_{n_e} and δ_{T_e} satisfy the conditions $|\delta_{n_e}| \leqslant 1$ and $|\delta_{T_e}| \leqslant 1$. The plasma resistivity is inversely related to the electron temperature (minimum resistivity is defined by the maximum electron temperature), and the resistivity range is shown in figure 5(*c*). Additionally, the parameters $\sqrt{T_e}$ and $1/n_e$ (note that $j_{nbi} \propto \sqrt{T_e}/n_e$ and $j_{ec} \propto T_e/n_e$ (see (13))) are related to the electron temperature and density, respectively. For feedback control design, these parameters are modeled as

$$\eta(\hat{\rho}) = \eta^{nom}(\hat{\rho}) + \eta^{unc}(\hat{\rho})\delta_{T_e}, \tag{41}$$

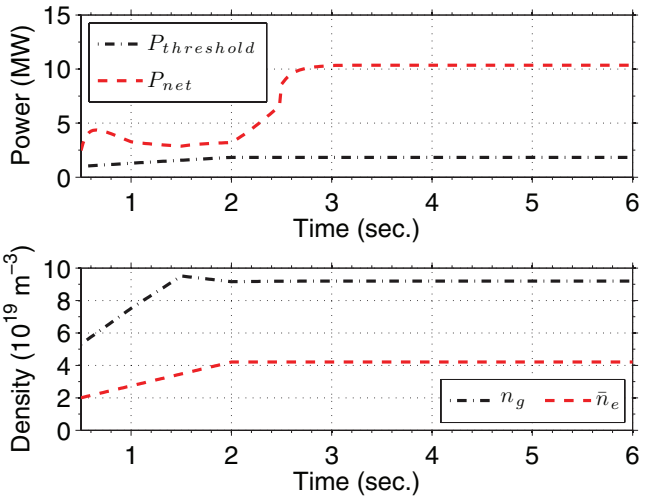

Figure 3. H-mode threshold (32) and density limit (33) conditions achieved with the actuator trajectories shown in figure 2 that are obtained by solving the optimization problem (36)–(37).

$$\sqrt{T_{\rm e}(\hat{\rho})} = T_{\rm e}^{\rm nom'}(\hat{\rho}) + T_{\rm e}^{\rm unc'}(\hat{\rho})\delta_{T_{\rm e}}, \tag{42}$$

$$1/n_{\rm e}(\hat{\rho}) = n_{\rm e}^{\rm nom'}(\hat{\rho}) + n_{\rm e}^{\rm unc'}(\hat{\rho})\delta_{n_{\rm e}}, \tag{43}$$

where the nominal ($\eta^{\rm nom}$, $T_{\rm e}^{\rm nom'}$, $n_{\rm e}^{\rm nom'}$) and uncertain ($\eta^{\rm unc}$, $T_{\rm e}^{\rm unc'}$, $n_{\rm e}^{\rm unc'}$) profiles are defined in terms of the maximum and minimum profiles shown in figure 5. The plasma resistivity and $\sqrt{T_{\rm e}}$ dependence on the electron temperature is modeled to first order to simplify the feedback control design process.

Combining the magnetic diffusion equation (4) with the noninductive current-drive models (12)–(14) and the uncertain models (39)–(43), we obtain the PDE model of the poloidal magnetic flux dynamics used for feedback control design, which is expressed as

$$\begin{aligned}\frac{\partial\psi}{\partial t} &= \frac{(\eta^{\rm nom}+\eta^{\rm unc}\delta_{T_{\rm e}})}{\mu_0\rho_b^2\hat{F}^2}\frac{1}{\hat{\rho}}\frac{\partial}{\partial\hat{\rho}}\left(\hat{\rho}\hat{F}\hat{G}\hat{H}\frac{\partial\psi}{\partial\hat{\rho}}\right)\\ &+ R_0\hat{H}(\eta^{\rm nom}+\eta^{\rm unc}\delta_{T_{\rm e}})\{n_{\rm e}^{\rm nom'}+n_{\rm e}^{\rm unc'}\delta_{n_{\rm e}}\}\\ &\times\Bigg[(T_{\rm e}^{\rm nom}+T_{\rm e}^{\rm unc}\delta_{T_{\rm e}})j_{{\rm ec}_{\rm tot}}^{\rm ref}P_{{\rm ec}_{\rm tot}}(t)\\ &+(T_{\rm e}^{\rm nom'}+T_{\rm e}^{\rm unc'}\delta_{T_{\rm e}})\left(\sum_i j_i^{\rm ref}P_i(t)\right)\Bigg]\\ &+\frac{k_{\rm J\,keV}R_0^2\hat{H}(\eta^{\rm nom}+\eta^{\rm unc}\delta_{T_{\rm e}})}{\hat{F}}\left(\frac{\partial\psi}{\partial\hat{\rho}}\right)^{-1}\\ &\times\Bigg[2\mathcal{L}_{31}(T_{\rm e}^{\rm nom}+T_{\rm e}^{\rm unc}\delta_{T_{\rm e}})\frac{\partial}{\partial\hat{\rho}}\{n_{\rm e}^{\rm nom}+n_{\rm e}^{\rm unc}\delta_{n_{\rm e}}\}\\ &+\{2\mathcal{L}_{31}+\mathcal{L}_{32}+\alpha\mathcal{L}_{34}\}\\ &\times\{n_{\rm e}^{\rm nom}+n_{\rm e}^{\rm unc}\delta_{n_{\rm e}}\}\frac{\partial}{\partial\hat{\rho}}\{T_{\rm e}^{\rm nom}+T_{\rm e}^{\rm unc}\delta_{T_{\rm e}}\}\Bigg],\end{aligned} \tag{44}$$

where $i\in\{{\rm nbi}_{\rm 30L/R}, {\rm nbi}_{\rm 150L/R}, {\rm nbi}_{\rm 330L/R}\}$. Additionally, for feedback control design, the plasma stored energy dynamics (6) are approximated as

$$\frac{{\rm d}E}{{\rm d}t} = -\frac{E}{\tau_{\rm E}(t)} + P_{\rm aux}(t) = -\frac{E}{\tau_{\rm E}(t)} + \sum_i P_i(t), \tag{45}$$

where $i\in\{{\rm ec}_{\rm tot}, {\rm nbi}_{\rm 30L/R}, {\rm nbi}_{\rm 150L/R}, {\rm nbi}_{\rm 330L/R}\}$. In (45), we have neglected the ohmic and radiated powers to simplify the feedback design as they are typically small compared to the auxiliary heating power in the scenarios considered. From (1), we see that the q profile is inversely related to the spatial gradient of the poloidal stream function, which we define as

$$\theta(\hat{\rho},t) \equiv \frac{\partial\psi}{\partial\hat{\rho}}(\hat{\rho},t), \tag{46}$$

and after some mathematical manipulations, a PDE governing the evolution of θ can be obtained from (44). In order to facilitate the feedback control design, the θ PDE is spatially discretized by employing a finite difference method to obtain an ordinary differential equation model defined by

$$\dot{\hat{\theta}} = f_\theta(\hat{\theta}, u, \delta), \tag{47}$$

where $\hat{\theta} = [\theta_2, \ldots, \theta_{m_\theta-1}]^{\rm T}\in\mathbb{R}^{n_\theta}$ is the magnetic state vector, θ_i, for $i = 2, \ldots, m_\theta - 1$, is the value of θ at the ith node, $u = [P_{{\rm ec}_{\rm tot}}, P_{{\rm nbi}_{\rm 30L/R}}, P_{{\rm nbi}_{\rm 150L/R}}, P_{{\rm nbi}_{\rm 330L/R}}, I_{\rm p}]^{\rm T}\in\mathbb{R}^8$ is the input vector, the uncertain parameter vector is $\delta = [\delta_{T_{\rm e}}, \delta_{n_{\rm e}}, \delta_{T_{\rm e}}\delta_{n_{\rm e}}, \delta_{T_{\rm e}}^2, \delta_{T_{\rm e}}^2\delta_{n_{\rm e}}]^{\rm T}\in\mathbb{R}^5$, $f_\theta\in\mathbb{R}^{n_\theta}$ is a nonlinear function of the plasma magnetic states, control inputs and uncertain parameters, $n_\theta = m_\theta - 2$ and m_θ is the number of equally spaced nodes used to represent the spatial domain. By defining the plasma state vector as $x = [\hat{\theta}, E]\in\mathbb{R}^{n_\theta+1}$, we can write the magnetic and kinetic state dynamics as

$$\dot{x} = \begin{bmatrix} f_\theta(\hat{\theta}, u, \delta) \\ -\dfrac{E}{\tau_{\rm E}(t)} + \sum_{i=1}^{7} u_i \end{bmatrix} = F_{\theta,E}(x, u, \delta)\in\mathbb{R}^{n_\theta+1}. \tag{48}$$

We define a nominal equilibrium point of the system (48) as

$$\dot{x}_{\rm eq} = F_{\theta,E}(x_{\rm eq}, u_{\rm eq}, 0) = 0, \tag{49}$$

and a model suitable for tracking control design can be obtained by defining the perturbation variables $\tilde{x}(t) = x(t) - x_{\rm eq}$ and $u_{\rm fb}(t) = u(t) - u_{\rm eq}$, where $\tilde{x}(t)$ is the deviation away from the equilibrium state and $u_{\rm fb}(t)$ is the output of the to-be-designed feedback controller. Linearizing (48) *with respect to the state (x) and control input (u)* around an equilibrium point defined by (49), we obtain

$$\dot{x}_{\rm eq} + \dot{\tilde{x}} = F_{\theta,E}(x_{\rm eq}, u_{\rm eq}, \delta) + \left.\frac{\partial F_{\theta,E}}{\partial x}\right|_{(x_{\rm eq},u_{\rm eq},\delta)}\tilde{x} + \left.\frac{\partial F_{\theta,E}}{\partial u}\right|_{(x_{\rm eq},u_{\rm eq},\delta)}u_{\rm fb}. \tag{50}$$

By employing (49), we express (50) as

$$\begin{aligned}\dot{\tilde{x}} &= A(\delta)\tilde{x} + B(\delta)u_{\rm fb} + d_\delta,\\ y &= \tilde{x},\end{aligned} \tag{51}$$

where $A(\delta)$ and $B(\delta)$ are the Jacobians $\partial F_{\theta,E}/\partial x$ and $\partial F_{\theta,E}/\partial u$ evaluated at $(x_{\rm eq}, u_{\rm eq}, \delta)$ and $d_\delta = F_{\theta,E}(x_{\rm eq}, u_{\rm eq}, \delta)$ is a disturbance. The model (51) contains the physics information of

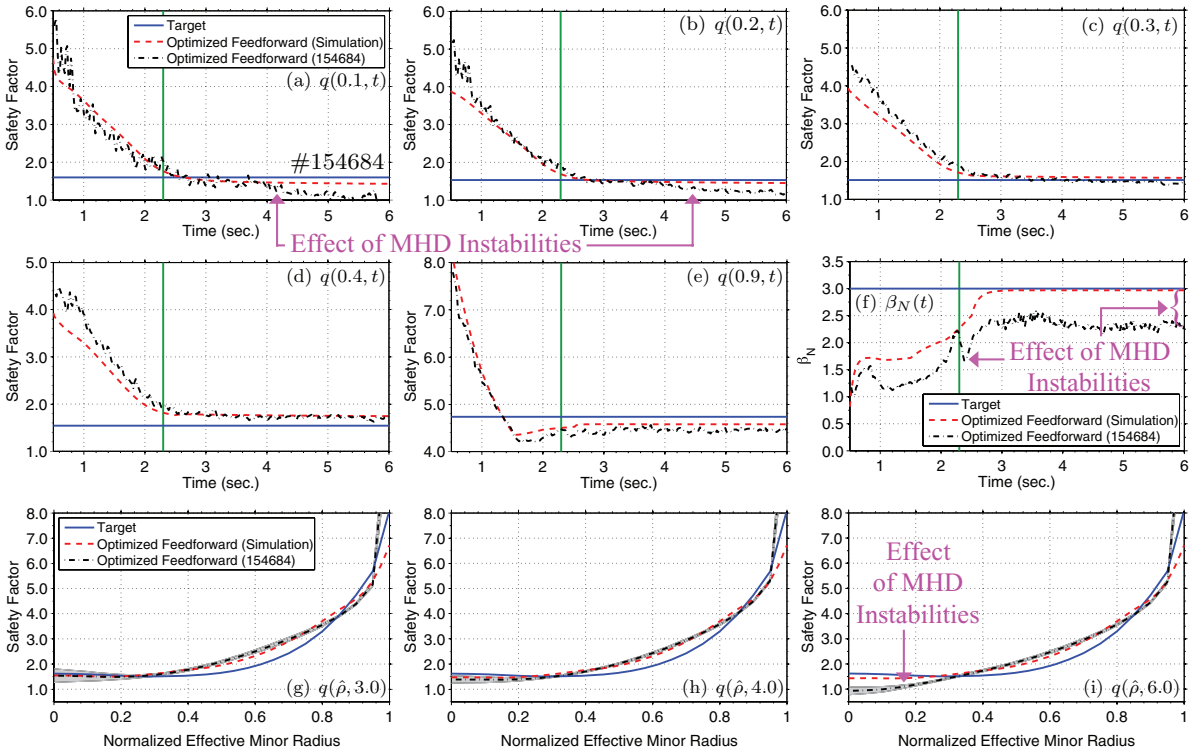

Figure 4. Simulated and experimental (DIII-D shot 154684) testing of optimized actuator trajectories: (*a*)–(*e*) time traces of q at $\hat{\rho} = 0.1, 0.2, 0.3, 0.4, 0.9$, (*f*) time trace of β_N, and (*g*)–(*i*) q profile at $t = 3.0$,4.0, and 6.0 s. The solid green line denotes the onset of MHD instabilities during DIII-D shot 154684. Approximate error bars for the measured q profiles (obtained from real-time EFIT (rtEFIT) [51]) are shown by the gray-shaded regions.

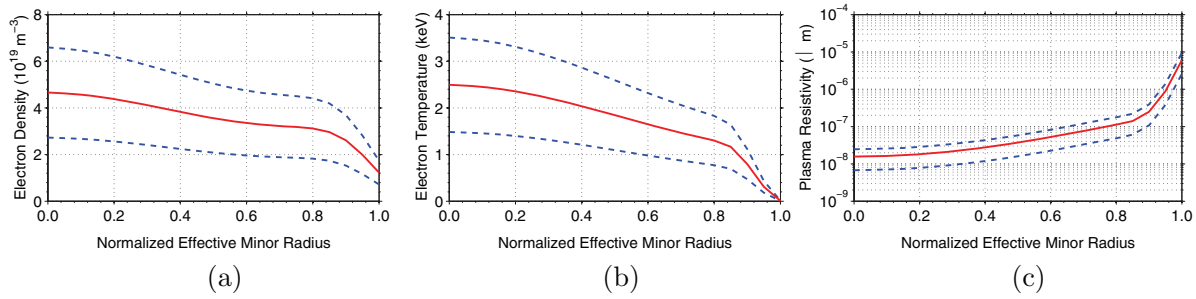

Figure 5. Plasma parameter uncertainty ranges in DIII-D H-mode scenarios: (*a*) electron density, (*b*) electron temperature, and (*c*) plasma resistivity. Nominal values, solid; minimum/maximum values, dashed.

how the control actuators, as well as the uncertain parameters δ_{n_e} and δ_{T_e}, influence the poloidal flux gradient profile and stored energy dynamics, and this information is embedded into the feedback controller by employing *robust control design techniques* [52].

The target plasma state evolution is prescribed by a reference vector $r(t)$, and it is desired that the system output $y(t)$ is driven to the target evolution. Therefore, we define the tracking error $e(t)$ as

$$e = r - y. \tag{52}$$

The feedback control objectives are to (i) maintain a small tracking error for any external reference input (r), (ii) reject the effects of any external disturbance input (d_δ) and (iii) utilize as little feedback control effort (u_{fb}) as possible. This control problem can be expressed mathematically as

$$\min_K \|T_{zw}\|_\infty, \tag{53}$$

where K is the feedback controller, the function T_{zw} represents the influence the parameters r and d_δ have on the parameters e and u_{fb} in closed-loop and $\|\cdot\|_\infty$ denotes the H_∞ norm [52]. Note that T_{zw} is dependent on both the system model (51) and the feedback controller K. The feedback controller is then obtained by solving (53). The controller is designed for tighter regulation of the q profile in the plasma core ($\hat{\rho} \in (0, 0.3]$) and near the plasma boundary ($\hat{\rho} \in [0.85, 1)$), as the q-value in these regions intimately affects plasma stability and performance. Additionally, the controller is designed to ensure that the closed-loop system remains stable for the ranges of the kinetic plasma parameters shown in figure 5, which provides confidence that the controller can be utilized in a variety of operating conditions. The interested reader is directed to [53, 54], where a mathematical derivation of (53) is provided.

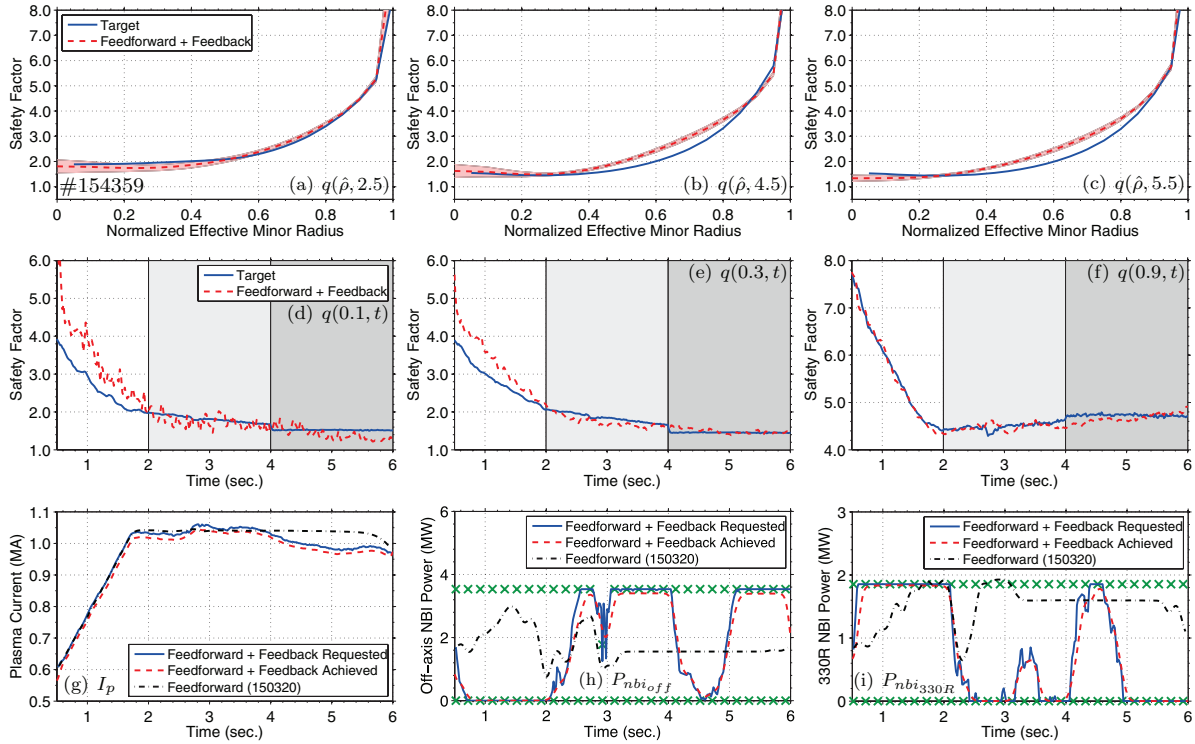

Figure 6. Experimental testing of q profile feedback controller during DIII-D shot 154359: (a)–(c) q profile at $t = 2.5$, 4.5, and 5.5 s, (d)–(f) time traces of q at $\hat{\rho} = 0.1, 0.3$, and 0.9, and (g)–(i) comparison of actuator trajectories ($P_{\mathrm{nbi_{off}}} = P_{\mathrm{nbi_{150L}}} + P_{\mathrm{nbi_{150R}}}$). Approximate error bars for the measured q profiles (obtained from rtEFIT [51]) are shown by the red-shaded regions. Actuator limits are denoted by the green cross.

5. Performance testing of *q* profile feedback control algorithm in DIII-D experiments

In this section, we test the ability of a q profile feedback control algorithm [53] (not including E feedback control) to reach, and subsequently maintain, a target safety factor profile in H-mode experiments in the DIII-D tokamak. While in future tokamak operation the objective will be to combine the optimal feedforward controller introduced in section 3 with the feedback controller presented in section 4, we employ in this section feedforward control inputs that are not optimal in order to facilitate the evaluation of the feedback controller performance. The q profile controller is designed by focusing on (47). To ensure that the closed-loop system remains well behaved in the presence of actuator magnitude saturation, the controller is augmented with an anti-windup compensator [55]. We employ the general framework for real-time feedforward + feedback control of magnetic plasma profiles implemented in the DIII-D plasma control system (PCS) [37] to test the control algorithm. The feedback controller is implemented with a sampling time of 20 ms based on the modulation of the 30L/R neutral beam sources (which are not used for feedback control, i.e. $u_{\mathrm{fb}} = 0$ for $P_{\mathrm{nbi_{30L/R}}}$) that are used to acquire diagnostic data to reconstruct the q profile using the rtEFIT equilibrium reconstruction code [51].

5.1. Reference tracking experimental testing of q profile controller

In a DIII-D discharge, robust tracking of a stationary target q profile was obtained in the presence of external plasma disturbances. In DIII-D shot 154359, the q profile feedback controller (not including E feedback control) was tested in a feedforward + feedback target tracking experiment. The target q profile ($q^{\mathrm{tar}}(\hat{\rho}, t)$) was obtained from the q profile achieved in DIII-D shot 150320 ($q^{320}(\hat{\rho}, t)$) as follows:

$$q^{\mathrm{tar}}(\hat{\rho}, t) = q^{320}(\hat{\rho}, t) \qquad \text{over } t \in [0.5, 2.0]\text{s},$$

$$q^{\mathrm{tar}}(\hat{\rho}, t) = q^{320}(\hat{\rho}, 2) + [q^{320}(\hat{\rho}, 5) - q^{320}(\hat{\rho}, 2)]\frac{(t-2)}{(5-2)}$$

$$\text{over } t \in (2.0, 4.0)\text{s},$$

$$q^{\mathrm{tar}}(\hat{\rho}, t) = q^{320}(\hat{\rho}, 5.0) \qquad \text{over } t \in [4.0, 6.0]\text{s}.$$

The feedforward component of the control input was chosen to be the actuator trajectories achieved in DIII-D shot 150320 ($I_{\mathrm{p}} \simeq 1.04$ MA, $B_{\phi,0} \simeq 1.66$ T, $q_{\mathrm{min}} \simeq 1.5$, $q_0 \simeq 1.6$, $q_{95} \simeq 5.1$, $\beta_{\mathrm{N}} \simeq 3.1$). Following the discussion in section 3.1, it must be said that another key physics goal of plasma profile control is to be able to robustly reproduce target scenarios and enable controlled variation of specific characteristics of the profiles through feedback to better elucidate physics.

A comparison of the target and experimentally achieved (154359) q profiles at various times, time traces of q at various radial locations and a comparison of the actuator trajectories are shown in figure 6. As shown, the controller was able to drive the q profile to the target (specifically in the spatial regions where the tracking performance was more heavily weighted ($\hat{\rho} \in (0, 0.3]$ and $\hat{\rho} \in [0.85, 1.0]$)) and achieve a relatively stationary condition in the presence of perturbations in the initial conditions and actuator regulation disturbances.

During the feedback-controlled discharge (154359), (1) the 30L/R neutral beam injectors were utilized at a constant power (total of 2 MW) to acquire diagnostic data, (2) the 330L neutral beam injector and the gyrotron launchers were unavailable for feedback control due to errors in the setup, (3) the 330L NBI delivered a constant 1.9 MW of power during the time interval $t \in [2.5, 6.0]$ s and (4) the gyrotrons delivered a constant 1.6 MW of power during the time interval $t \in [2.5, 3.0]$ s and a constant 1.2 MW during the time interval $t \in (3.0, 6.0)$ s. During the target discharge, (1) the power in the 30L/R neutral beam injectors was increased from a low value (total of 1.2 MW) to a high value (total of 3.2 MW) at 3.0 s, (2) the 330L NBI delivered a constant 1.7 MW of power during the time interval $t \in [2.5, 6.0]$ s and (3) the gyrotrons delivered a constant 2.8 MW of power during the time interval $t \in [2.5, 6.0]$ s. Additionally, the flattop line average electron density was approximately 5% lower in the feedback-controlled discharge (154359) than in the target discharge during the approximate time interval $t \in (3.7, 5.4)$ s. The controller utilized the total plasma current to regulate the q profile near the plasma boundary (figures 6(*f*) and (*g*)) and modulated the mix of the on-and-off axis auxiliary current drives that were available for feedback control to track the target q profile in the plasma core (figures 6(*d*), (*e*), (*h*) and (*i*)). First, during the time intervals $t \in [0.5, 2.0]$ s and $t \in (4.0, 5.0)$ s, the q-value in the plasma core was above the target. In response to this tracking error, the feedback controller decreased the off-axis neutral beam injection power ($P_{\mathrm{nbi}_{\mathrm{off}}}$) and increased the on-axis neutral beam power ($P_{\mathrm{nbi}_{330\mathrm{R}}}$) to track the target q profile in the plasma core. Second, during the time intervals $t \in (2.0, 4.0]$ s and $t \in [5.0, 6.0]$ s, the q-value in the plasma core was below the target. In response to this tracking error, the feedback controller increased the off-axis neutral beam injection power ($P_{\mathrm{nbi}_{\mathrm{off}}}$) and decreased the on-axis neutral beam power ($P_{\mathrm{nbi}_{330\mathrm{R}}}$) to track the target q profile in the plasma core. Finally, as shown in figure 7(*a*), the achieved β_{N} was relatively close to the target even though it was not feedback controlled. This resulted in similar bootstrap current profiles in the target and feedback-controlled (154359) discharges, as shown in figure 7(*b*).

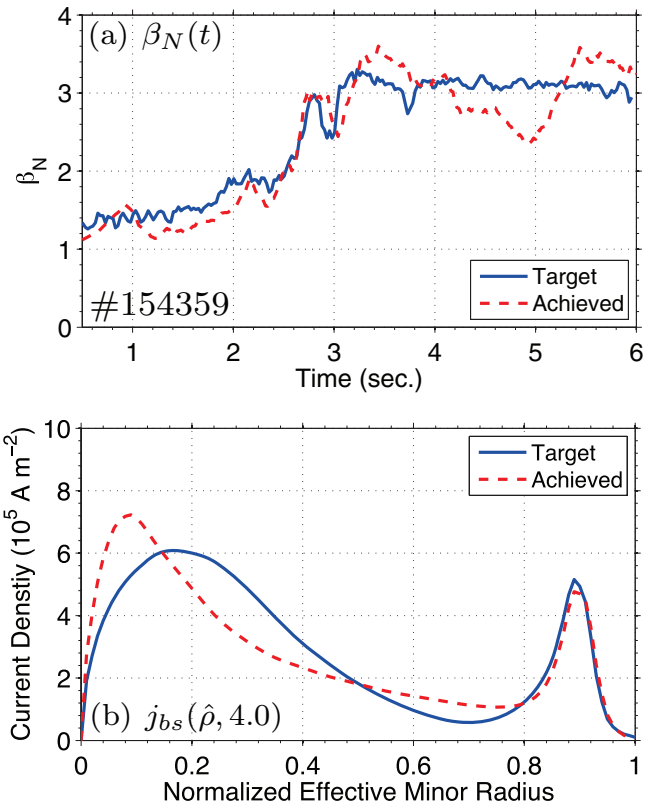

Figure 7. Comparison of (*a*) β_{N} and (*b*) bootstrap current profile j_{bs} (computed by TRANSP [8]) at 4.0 s. The bootstrap fraction in the target discharge was $f_{\mathrm{bs}} = 38\%$ and that in the feedback-controlled discharge (154359) was $f_{\mathrm{bs}} = 39\%$ at 4.0 s. The bootstrap fraction is defined as $f_{\mathrm{bs}} = I_{\mathrm{bs}}/I_{\mathrm{p}}$, where $I_{\mathrm{bs}} = \int_0^1 j_{\mathrm{bs}}(\hat{\rho}) \frac{\mathrm{d}S}{\mathrm{d}\hat{\rho}} \mathrm{d}\hat{\rho}$.

5.2. Disturbance rejection experimental testing of q profile controller

In another DIII-D discharge, rejection of a disturbance purposely introduced in the initial q profile was obtained exclusively through feedback actuation. In DIII-D shot 154692, the q profile feedback controller (not including E feedback control) was tested in a pure feedback disturbance rejection experiment. The q profile evolution achieved in DIII-D shot 154358 was chosen as the target ($I_{\mathrm{p}} \simeq 1.02$ MA, $B_{\phi,0} \simeq 1.68$ T, $q_{\mathrm{min}} \simeq 1.7$, $q_0 \simeq 1.9$, $q_{95} \simeq 5.25$, $\beta_{\mathrm{N}} \simeq 3.3$). A significant disturbance (low relative to the target) in the q profile at 0.5 s (when the feedback controller was turned on) was introduced to the plasma by delaying the time at which the plasma transitioned from the low confinement to the high confinement operating regime. This delay resulted in the inductive component of the plasma current profile diffusing in towards the center of the plasma at a faster rate than in the target shot. The feedforward component of the control input was frozen after 1.6 s; therefore, the achieved profile regulation was obtained exclusively through feedback.

A comparison of the target and experimentally achieved (154692) q profiles at various times, time traces of q at various radial locations and a comparison of the actuator trajectories are shown in figure 8. As shown in the figures, the controller was able to reject the effects of the initial condition error and drive the q profile to the target during the time interval $t \in [0.5, 3.5]$ s in the presence of actuator regulation disturbances. In the feedback-controlled discharge (154692) the gyrotrons were unavailable for feedback control due to errors in the setup and did not deliver any power to the plasma, while in the target discharge the gyrotrons delivered a constant 3 MW of power during the time interval $t \in [2.5, 6.0]$ s. Additionally, the flattop line average electron density in the feedback-controlled discharge (154692) was approximately 5–10% lower than in the target discharge during the approximate time interval $t \in (3.0, 5.0)$ s. Figures 8(*g*)–(*i*) also show that the feedforward control inputs were frozen after 1.6 s (feedforward I_{p} fixed at 0.8 MA and no feedforward modulation of the beam powers). The controller utilized the actuators to regulate the q profile across the spatial domain in the same way as in the previously discussed feedback

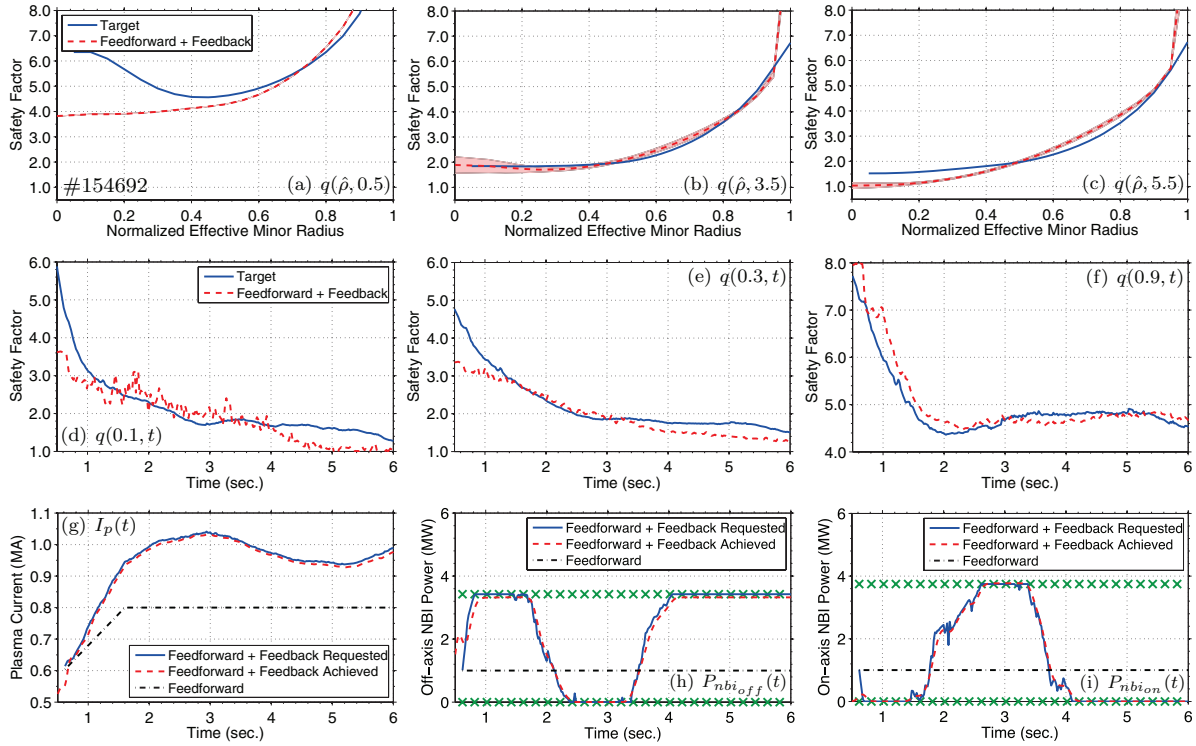

Figure 8. Experimental testing of q profile feedback controller during DIII-D shot 154692: (*a*)–(*c*) q profile at $t = 0.5$,3.5 and 5.5 s, (*d*)–(*f*) time traces of q at $\hat{\rho} = 0.1, 0.3$ and 0.9, and (*g*)–(*i*) comparison of actuator trajectories ($P_{\text{nbi}_{\text{on}}} = P_{\text{nbi}_{330\text{L}}} + P_{\text{nbi}_{330\text{R}}}$). Approximate error bars for the measured q profiles (obtained from rtEFIT [51]) are shown by the red-shaded regions. Actuator limits are denoted by the green cross.

experiment (figures 8(*d*)–(*i*)). However, even though the controller requested the maximum amount of off-axis auxiliary current drive during the time interval $t \in [4.0, 6.0]$ s, the q profile in the plasma core was unable to be maintained at the target. As shown in figure 9(*a*), the achieved β_N was relatively far away from the target during the time interval $t \in (3.0, 5.5]$ s. This resulted in a lower bootstrap current profile in the feedback-controlled discharge (154692) relative to the target as shown in figure 9(*b*). As the bootstrap current is an off-axis source of current, a lower bootstrap current may have contributed to the inability to maintain the q profile in the plasma core at the target during the feedback-controlled experiment (154692).

6. Simulation testing of integrated q profile + E controller

In the previous section, the q profile controller was shown to be able to effectively control the q profile when β_N is relatively close to the target. This indicates that an important aspect of achieving robust scenario execution is the need to simultaneously achieve a target q profile and β_N. In this section, a q profile + E feedback controller [53] is tested through simulations based on the physics-based model of the plasma poloidal magnetic flux profile and stored energy dynamics described in section 2. The integrated controller is designed by focusing on (48). First, a target q profile and β_N evolution is obtained by executing a feedforward-only simulation with the control input trajectories and initial conditions ($q(\hat{\rho}, 0.5)$

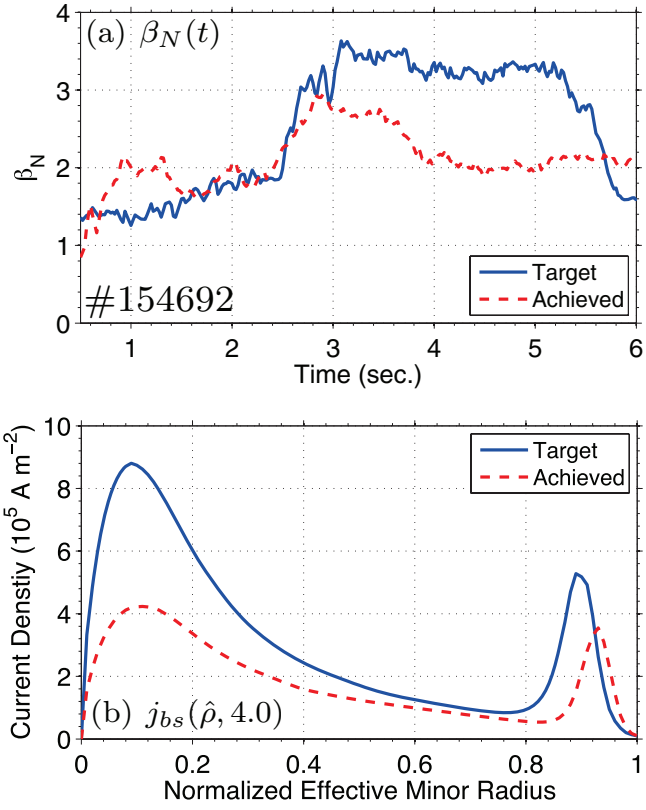

Figure 9. Comparison of (*a*) β_N and (*b*) bootstrap current profile (computed by TRANSP [8]) at 4.0 s. The bootstrap fraction in the target discharge was $f_{\text{bs}} = 39\%$ and that in the feedback-controlled discharge (154692) was $f_{\text{bs}} = 27\%$ at 4.0 s.

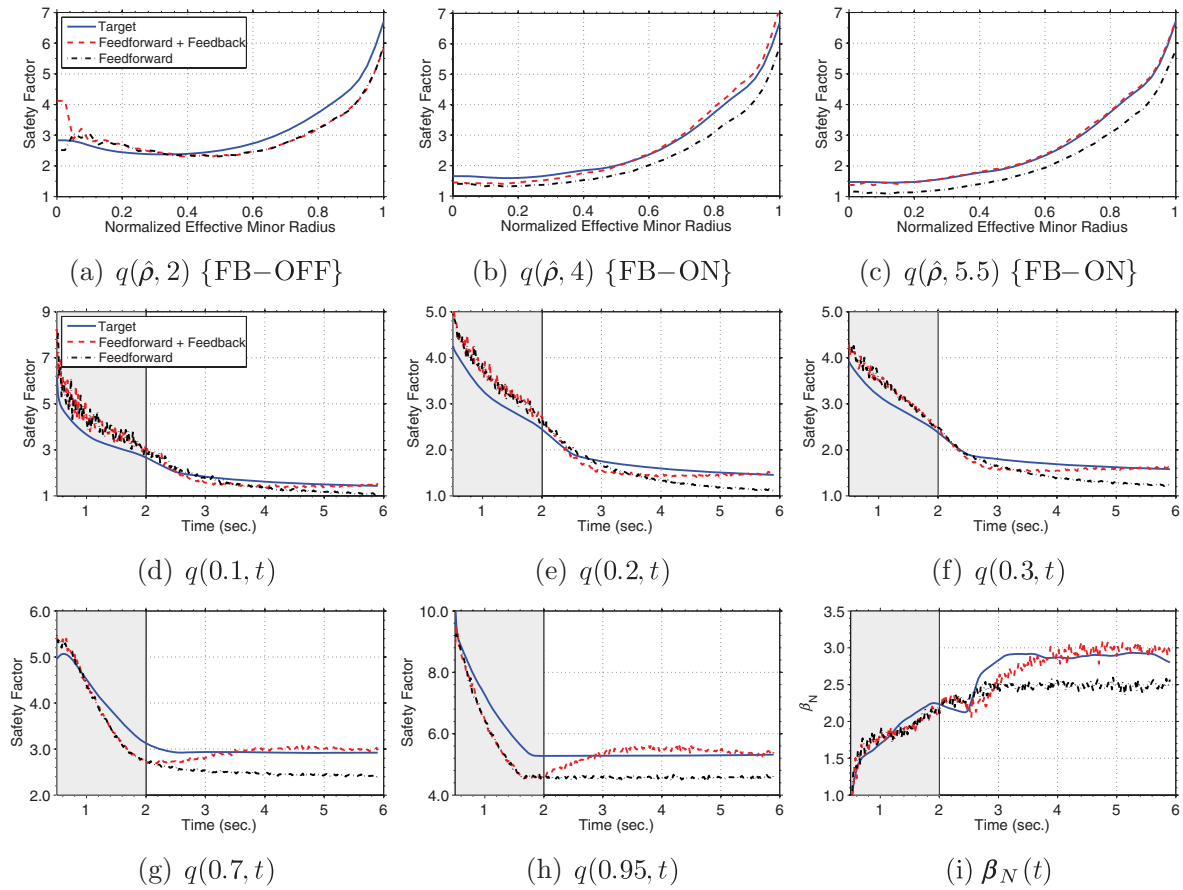

Figure 10. Simulation testing of q profile + E feedback controller: (*a*)–(*c*) q profile at various times, (*d*)–(*h*) time trace of q at various spatial locations, and (*i*) time trace of plasma β_N. The gray-shaded region indicates when the feedback controller is inactive. (*a*) $q(\hat{\rho}, 2)$ {FB–OFF}. (*b*) $q(\hat{\rho}, 4)$ {FB–ON}. (*c*) $q(\hat{\rho}, 5.5)$ {FB–ON}. (*d*) $q(0.1,t)$. (*e*) $q(0.2,t)$. (*f*) $q(0.3,t)$. (*g*) $q(0.7,t)$. (*h*) $q(0.95,t)$. (*i*) $\beta_N(t)$.

and $\beta_N(0.5)$) achieved in DIII-D shot 150318 ($I_p \simeq 1.04$ MA, $B_{\phi,0} \simeq 1.66$ T, $q_{min} \simeq 1.5$, $q_0 \simeq 1.6$, $q_{95} \simeq 5.2$, $\beta_N \simeq 3.1$). Second, a nominal q profile and β_N evolution is obtained by executing a feedforward-only simulation with a nominal set of input trajectories and initial conditions. Finally, the ability of the algorithm to track the target evolutions that are obtained from the first simulation is determined by executing a feedforward + feedback simulation with the nominal input trajectories and initial conditions that are used in the second simulation. During the feedback-controlled simulation, the controller is inactive during the time interval $t = [0.5,2.0]$ s. Simulated white noise is added to both the feedforward + feedback and feedforward simulations to approximately replicate the noise level observed in the rtEFIT measurements during DIII-D operations.

A comparison of the target, feedforward + feedback controlled and feedforward controlled q profiles at various times, time traces of q at various spatial locations and a time trace of the plasma β_N are shown in figure 10. A comparison of the control inputs is shown in figure 11. As shown in the figures, the controller is able to drive the q profile and plasma β_N to the target evolutions once it becomes active at 2.0 s in the presence of perturbations in the initial conditions and actuator regulation disturbances. During the feedback-controlled simulation the 30L/R neutral beam injectors were utilized at a constant power, while during the target simulation the power in these beams was increased from a low value to a high value at 3.0 s (see figures 11(*d*) and (*e*)). Additionally, during the feedback-controlled simulation, the flattop line average electron density was approximately 5–10% higher than in the target simulation (see figure 11(*b*)). In the feedback-controlled simulation, first, the controller decreases the total plasma current to eliminate the error in q near the plasma boundary (see figures 10(*g*) and (*h*) and 11(*a*)). Second, at approximately 2.5 s, the value of q in the plasma core evolves below the target value. In response, the controller decreases the on-axis auxiliary current drive ($P_{\mathrm{nbi}_{330L/R}}$) and increases the off-axis auxiliary current drive ($P_{\mathrm{ec}_{tot}}$ and $P_{\mathrm{nbi}_{150L/R}}$) to track the target q profile in the plasma core (see figures 10(*d*)–(*f*), 11(*c*) and (*f*)–(*i*)). Finally, in order to track the target plasma β_N while maintaining good tracking of the q profile in the plasma core, the controller slowly increases the on-axis auxiliary heating (specifically $P_{\mathrm{nbi}_{330R}}$) beginning at approximately 3.25 s.

7. Conclusions and discussion

The reported advances demonstrate the potential that the physics-model-based profile control has to provide a systematic approach for the development and robust sustainment of advanced scenarios in DIII-D. These control algorithms also enable detailed study of the accuracy and validity of

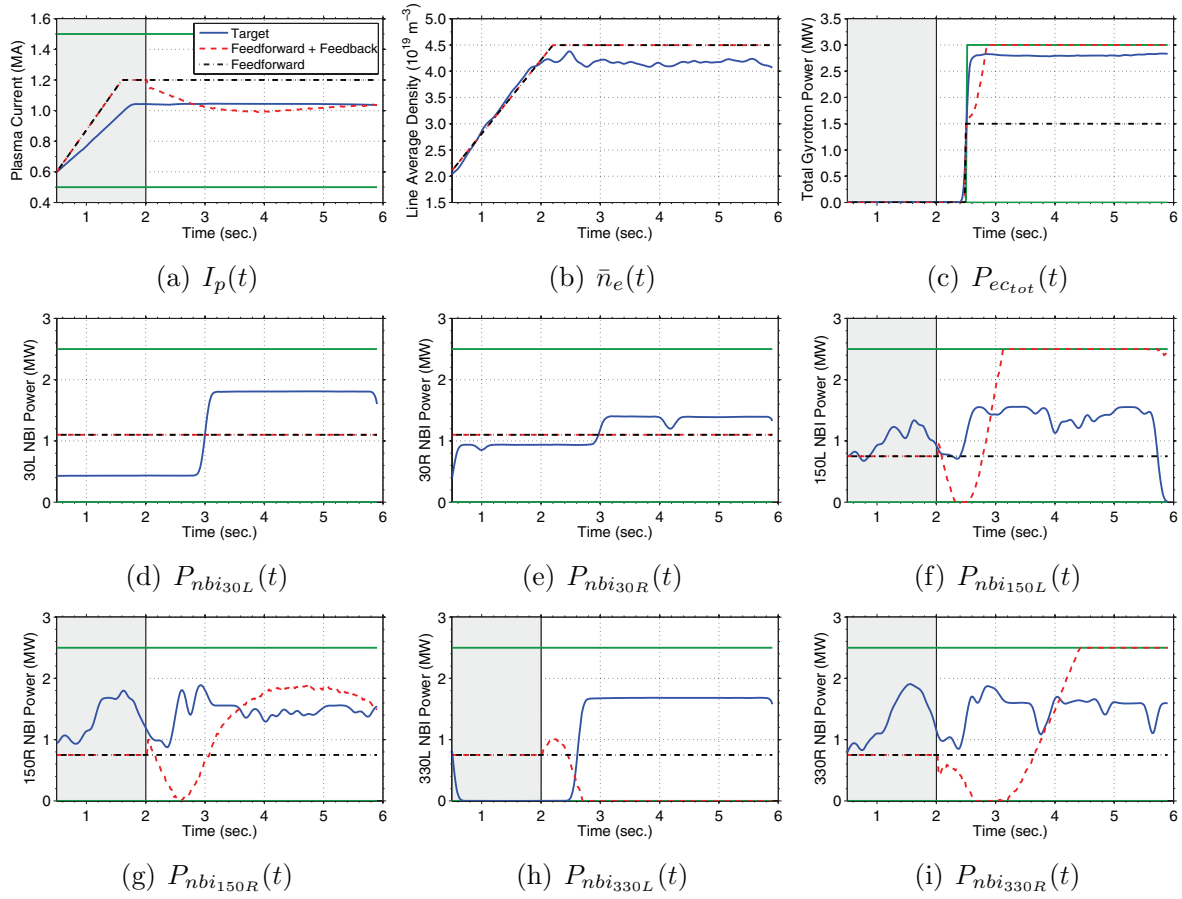

Figure 11. Simulation testing of q profile + E feedback controller: actuator trajectory comparison (actuator limits in solid green). The shaded gray region denotes when the feedback controller is not active. Note that the gyrotrons become available at 2.5 s and that the line average electron density and the 30L/R neutral beam lines are not feedback controlled. (*a*) $I_p(t)$. (*b*) $\bar{n}_e(t)$. (*c*) $P_{ec_{tot}}(t)$. (*d*) $P_{nbi_{30L}}(t)$. (*e*) $P_{nbi_{30R}}(t)$. (*f*) $P_{nbi_{150L}}(t)$. (*g*) $P_{nbi_{150R}}(t)$. (*h*) $P_{nbi_{330L}}(t)$. (*i*) $P_{nbi_{330R}}(t)$.

the relevant models themselves and can help clarify physics aspects important to robust scenario execution. A numerical optimization algorithm was developed to complement the experimental effort of advanced scenario planning in the DIII-D tokamak. At the core of the optimization algorithm is a nonlinear, physics-based, control-oriented model of the plasma dynamics. One direction of future work is to extend the physics-based model by coupling the poloidal magnetic flux profile dynamics with the distributed dynamics of the electron temperature profile in order to better represent the effect the q profile has on plasma transport [56]. The optimized actuator trajectories were successfully tested through simulation, and an experimental test in DIII-D demonstrated the ability of the optimized trajectories to steer the plasma to a target stationary q profile. However, as observed in the experimental test, access to advanced scenarios can be limited by triggering MHD instabilities. Therefore, a second direction of future work is to formulate additional plasma state constraints that can be imposed on the optimization problem solution to maintain distance from critical MHD stability limits, such as classical and neoclassical tearing modes.

As a result of the MHD instabilities that developed during the experimental test, the optimized feedforward trajectories were not able to achieve the target β_N and maintain a stationary q profile for the entirety of the plasma discharge. Therefore to account for external plasma disturbances and actuation limitations, a feedback control scheme was developed to control the q profile. The feedback controller was designed to be robust to uncertainties in the electron density, the electron temperature and the plasma resistivity, which provides confidence that the controller can be used in a variety of operating conditions. In this work, uncertainties in the plasma resistivity due to variations in the electron temperature were considered. Uncertainties in the plasma resistivity due to variations in Z_{eff}, as well as uncertainties in the energy confinement (represented by an uncertain $H_{H98(y,2)}$ factor), could be incorporated into the formulation of the control design problem in a relatively straightforward manner. The ability of the q profile feedback controller (not including energy control) to improve the ability to robustly achieve plasma target conditions was tested in DIII-D experiments. The q profile controller was shown to be able to effectively control the q profile when β_N is relatively close to the target. Therefore, these experiments indicate that another important aspect of achieving robust scenario execution is the need to simultaneously achieve a target q profile and β_N. Through simulations, the ability of an integrated q profile and stored energy feedback controller to track a desired target was demonstrated. Another direction of future work is to experimentally test the performance of the combined q profile and stored energy controller in DIII-D experiments.

The development of these profile control capabilities not only may help achieve physics objectives on DIII-D, but also will help to evaluate a control scheme that potentially can be utilized in future experiments and fusion power plants. The control scheme developed in this work is readily adaptable to a given operating scenario in a given machine of interest due to the strong first-principles dependence of the modeling and design approach used to synthesize controllers. The developed feedforward + feedback scheme has been employed to improve the reproducibility of plasma startup conditions on DIII-D by achieving a specified target q profile at the end of the current ramp-up phase [54, 57]. Additionally, feedback algorithms for profile control have been developed for tracking of q profile targets in NSTX-U H-mode scenarios [58] and in TCV L-mode scenarios [54, 59], simultaneous tracking of q profile and β_N targets in ITER burning plasma H-mode scenarios [54, 60] and simultaneous tracking of q profile and T_e profile targets in TCV L-mode scenarios [54, 61].

Acknowledgments

This material is based upon work partly supported by the US Department of Energy, Office of Science, Office of Fusion Energy Sciences, using the DIII-D National Fusion Facility, a DOE Office of Science user facility, under awards DE-SC0001334, DE-SC0010661, DE-AC05-00OR23100, DE-FC02-04ER54698 and DE-FG02-04ER54761.

Appendix A. Overview of sequential quadratic programming

We provide an overview of the SQP solution method for a general NLP defined by

$$\min_{v} \quad \mathcal{J}(z, v), \tag{A.1}$$

such that

$$f(z, v) = 0, \tag{A.2}$$

where $\mathcal{J}$ is a scalar-valued function to be minimized, z is the system state, v is the manipulated control input and f is a general nonlinear function. To simplify the explanation of the SQP technique, we only consider equality constraints in the form of (A.2). We begin by defining the system Hamiltonian as

$$\mathcal{H}(z, v, \lambda) = \mathcal{J}(z, v) + \lambda^T f(z, v), \tag{A.3}$$

where λ is a to-be-determined Lagrange multiplier. An incremental change in the Hamiltonian with respect to changes in the parameters is given to first order by

$$\mathrm{d}\mathcal{H} = \mathcal{H}_z \mathrm{d}z + \mathcal{H}_v \mathrm{d}v + \mathcal{H}_\lambda \mathrm{d}\lambda, \tag{A.4}$$

where $(\cdot)_i = \frac{\partial(\cdot)}{\partial i}$ for $i \in [z, v, \lambda]$. At a local minimum (z^*, v^*, λ^*), $\mathrm{d}\mathcal{H}$ must be zero for all increments $\mathrm{d}z$, $\mathrm{d}v$, $\mathrm{d}\lambda$. Therefore, the first-order optimality conditions for the NLP (A.1)–(A.2) are given by the nonlinear equations

$$\begin{aligned}
\mathcal{H}_z(z^*, v^*, \lambda^*) &= \mathcal{J}_z(z^*, v^*) + (\lambda^*)^T f_z(z^*, v^*) = 0,\\
\mathcal{H}_v(z^*, v^*, \lambda^*) &= \mathcal{J}_v(z^*, v^*) + (\lambda^*)^T f_v(z^*, v^*) = 0,\\
\mathcal{H}_\lambda(z^*, v^*, \lambda^*) &= f(z^*, v^*) = 0.
\end{aligned} \tag{A.5}$$

One approach to solving the NLP (A.1)–(A.2) is to assume we have an iteration

$$\begin{aligned}
(z^{(k+1)}, v^{(k+1)}, \lambda^{(k+1)}) = (z^{(k)}, v^{(k)}, \lambda^{(k)})\\
+ (\zeta^{(k)}, \xi^{(k)}, \sigma^{(k)})
\end{aligned}$$

that is converging to the solution (z^*, v^*, λ^*) of (A.5), where $(\zeta^{(k)}, \xi^{(k)}, \sigma^{(k)})$ are search directions. Assuming the current estimate $(z^{(k)}, v^{(k)}, \lambda^{(k)})$ is close to (z^*, v^*, λ^*), we can linearize (A.5) around the current estimate, i.e.

$$\begin{aligned}
0 &= \mathcal{H}_z(z^{(k)}, v^{(k)}, \lambda^{(k)}) + \mathcal{H}_{zz}(z^{(k)}, v^{(k)}, \lambda^{(k)})\zeta^{(k)}\\
&\quad + \mathcal{H}_{zv}(z^{(k)}, v^{(k)}, \lambda^{(k)})\xi^{(k)} + \mathcal{H}_{z\lambda}(z^{(k)}, v^{(k)}, \lambda^{(k)})\sigma^{(k)},\\
0 &= \mathcal{H}_v(z^{(k)}, v^{(k)}, \lambda^{(k)}) + \mathcal{H}_{vz}(z^{(k)}, v^{(k)}, \lambda^{(k)})\zeta^{(k)}\\
&\quad + \mathcal{H}_{vv}(z^{(k)}, v^{(k)}, \lambda^{(k)})\xi^{(k)} + \mathcal{H}_{v\lambda}(z^{(k)}, v^{(k)}, \lambda^{(k)})\sigma^{(k)},\\
0 &= \mathcal{H}_\lambda(z^{(k)}, v^{(k)}, \lambda^{(k)}) + \mathcal{H}_{\lambda z}(z^{(k)}, v^{(k)}, \lambda^{(k)})\zeta^{(k)}\\
&\quad + \mathcal{H}_{\lambda v}(z^{(k)}, v^{(k)}, \lambda^{(k)})\xi^{(k)} + \mathcal{H}_{\lambda\lambda}(z^{(k)}, v^{(k)}, \lambda^{(k)})\sigma^{(k)},
\end{aligned} \tag{A.6}$$

where $(\cdot)_{ij} = \frac{\partial^2(\cdot)}{\partial i \partial j}$ for $i \in [z, v, \lambda]$ and $j \in [z, v, \lambda]$. From (A.5), we note that

$$\mathcal{H}_{z\lambda} = \mathcal{H}_{\lambda z} = f_z \qquad \mathcal{H}_{v\lambda} = \mathcal{H}_{\lambda v} = f_v \qquad \mathcal{H}_{\lambda\lambda} = 0,$$

which allows us to write (A.6) in matrix form as

$$\begin{aligned}
&\begin{bmatrix} \mathcal{H}_{zz} & \mathcal{H}_{zv} & f_z \\ \mathcal{H}_{vz} & \mathcal{H}_{vv} & f_v \\ f_z & f_v & 0 \end{bmatrix}\Bigg|_{(z^{(k)}, v^{(k)}, \lambda^{(k)})} \begin{bmatrix} \zeta^{(k)} \\ \xi^{(k)} \\ \sigma^{(k)} \end{bmatrix}\\
&\quad = -\begin{bmatrix} H_z \\ H_v \\ f \end{bmatrix}\Bigg|_{(z^{(k)}, v^{(k)}, \lambda^{(k)})}.
\end{aligned} \tag{A.7}$$

The search directions $(\zeta^{(k)}, \xi^{(k)}, \sigma^{(k)})$ can then be obtained by solving (A.7). It can be shown that the first-order optimality condition of the QP

$$\min_{\xi^{(k)}} \quad \mathcal{L}(\zeta^{(k)}, \xi^{(k)})|_{(z^{(k)}, v^{(k)}, \lambda^{(k)})}, \tag{A.8}$$

such that

$$f(z^{(k)}, v^{(k)}) + \begin{bmatrix} f_z & f_v \end{bmatrix}\Big|_{(z^{(k)}, v^{(k)})} \begin{bmatrix} \zeta^{(k)} \\ \xi^{(k)} \end{bmatrix} = 0, \tag{A.9}$$

where

$$\mathcal{L} = \mathcal{H} + \begin{bmatrix} \mathcal{H}_z & \mathcal{H}_v \end{bmatrix}\begin{bmatrix} \zeta^{(k)} \\ \xi^{(k)} \end{bmatrix} + \frac{1}{2}\begin{bmatrix} \zeta^{(k)} & \xi^{(k)} \end{bmatrix}\begin{bmatrix} \mathcal{H}_{zz} & \mathcal{H}_{zv} \\ \mathcal{H}_{vz} & \mathcal{H}_{vv} \end{bmatrix}\begin{bmatrix} \zeta^{(k)} \\ \xi^{(k)} \end{bmatrix},$$

with Lagrange multiplier $\sigma^{(k)}$, is given by (A.7). Therefore from the sequence of quadratic programs (A.8)–(A.9)

(denoted as $QP^{(k)}$), which represent a quadratic approximation of $\mathcal{H}$ subject to a linear approximation of f around the current estimate $(z^{(k)}, \nu^{(k)}, \lambda^{(k)})$, search directions for the original NLP (A.1)–(A.2) can be obtained.

References

[1] Taylor T. *et al* 1997 Physics of advanced tokamaks *Plasma Phys. Control. Fusion* **39** B47–73

[2] Peeters A.G. 2000 The bootstrap current and its consequences *Plasma Phys. Control. Fusion* **42** B231–42

[3] Gormezano C. *et al* 2007 Progress in the ITER Physics Basis. Chapter 6: Steady state operation *Nucl. Fusion* **47** S285

[4] Waltz R.E. 1995 Advances in the simulation of toroidal gyro-landau fluid model turbulence *Phys. Plasmas* **2** 2408

[5] Petty C.C. 1998 Experimental constraints on transport from dimensionless parameter scaling studies *Phys. Plasmas* **5** 1695

[6] Ferron J. *et al* 2005 Optimization of DIII-D advanced tokamak discharges with respect to the β limit *Phys. Plasmas* **12** 056126

[7] Hender T.C. 2007 Progress in the ITER physics basis chapter 3: MHD stability, operational limits and disruptions *Nucl. Fusion* **47** S128–S202

[8] Hawryluk R.J. *et al* 1980 An empirical approach to tokamak transport *Physics of Plasmas Close to Thermonuclear Conditions* vol 1 , ed Coppi B *et al* (Oxford: Pergamon) pp 19–46

[9] John H.S., Taylor T.S., Turnbull A.D. and Lin-Liu Y.R. 1995 Transport simulation of negative magnetic shear discharges *Proc. 15th Int. Conf. on Plasma Physics and Controlled Nuclear Fusion Research (Seville, 26 Sept–1 Oct 1994)* (Vienna: IAEA) p 603 www.iaea.org/inis/collection/NCLCollectionStore/Public/27/058/27058544.pdf

[10] Crotinger J. *et al* 1997 *Technical Report* UCRL-ID-126284 LLNL

[11] Nocedal J. and Wright S.J. 2006 *Numerical Optimization* (New York: Springer)

[12] Ou Y. *et al* 2007 Towards model-based current profile control at DIII-D *Fusion Eng. Des.* **82** 1153–60

[13] Witrant E. *et al* 2007 A control-oriented model of the current profile in tokamak plasma *Plasma Phys. Control. Fusion* **49** 1075–105

[14] Felici F. *et al* 2011 Real-time physics-model-based simulation of the current density profile in tokamak plasmas *Nucl. Fusion* **51** 083052

[15] Ou Y. *et al* 2008 Design and simulation of extremum-seeking open-loop optimal control of current profile in the DIII-D tokamak *Plasma Phys. Control. Fusion* **50** 115001

[16] Xu C. *et al* 2010 Ramp-up phase current profile control of tokamak plasmas via nonlinear programming *IEEE Trans. Plasma Sci.* **38** 163–73

[17] Felici F. *et al* 2012 Nonlinear model-based optimization of actuator trajectories for tokamak plasma profile control *Plasma Phys. Control. Fusion* **54** 025002

[18] Moreau D. *et al* 2003 Real-time control of the q-profile in JET for steady state advanced tokamak operation *Nucl. Fusion* **43** 870–82

[19] Moreau D. *et al* 2008 A Two-time-scale dynamic-model approach for magnetic and kinetic profile control in advanced tokamak scenarios on JET *Nucl. Fusion* **48** 106001

[20] Shi W. *et al* 2012 Multivariable robust control of the plasma rotational transform profile for advanced tokamak scenarios in DIII-D *American Control Conf. Proc.* (*Montreal*, *27–29 June 2012*) pp 5037–42 doi: 10.1109/ACC.2012.6315411

[21] Wehner W. *et al* 2012 Optimal feedback control of the poloidal magnetic flux profile in the DIII-D tokamak based on identified plasma response models *American Control Conf. Proc.* (*Montreal*, *27–29 June 2012*) pp 5049–54 doi: 10.1109/ACC.2012.6315581

[22] Shi W. *et al* 2012 A two-time-scale model-based combined magnetic and kinetic control system for advanced tokamak scenarios on DIII-D *Proc. 51st IEEE Conf. on Decision and Control* (*Maui, HI*, *10–13 December 2012*) pp 4347–52 doi: 10.1109/CDC.2012.6426330

[23] Moreau D. *et al* 2012 Integrated magnetic and kinetic control of advanced tokamak scenarios based on data-driven models *Proc. 24th Int. Conf. on IAEA Fusion Energy* (*San Diego, CA*, *8–13 October 2012*) ITR/P1-20 www-naweb.iaea.org/napc/physics/FEC/FEC2012/papers/110 ITRP120.pdf

[24] Shi W. *et al* 2013 PTRANSP simulation and experimental test of a robust current profile and β_N controller for off-axis current-drive scenarios in the DIII-D tokamak *American Control Conf. Proc.* (*Washington DC*, *17–19 June 2013*) pp 1225–30 doi: 10.1109/ACC.2013.6580003

[25] Moreau D. *et al* 2013 Integrated magnetic and kinetic control of advanced tokamak plasmas on DIII-D based on data-driven models *Nucl. Fusion* **53** 063020

[26] Ou Y. and Schuster E. 2010 On stability of receding horizon control of bilinear parabolic PDE systems *Proc. 49th IEEE Conf. on Decision and Control* (*Atlanta, GA*, *15–17 December 2010*) doi: 10.1109/CDC.2010.5717938

[27] Ou Y., Xu C. and Schuster E. 2010 Robust control design for the poloidal magnetic flux profile evolution in the presence of model uncertainties *IEEE Trans. Plasma Sci.* **38** 375–82

[28] Ou Y., Xu C. and Schuster E. 2011 Optimal tracking control of current profile in tokamaks *IEEE Trans. Control Syst. Technol.* **19** 432–41

[29] Xu C., Ou Y. and Schuster E. 2011 Sequential linear quadratic control of bilinear parabolic PDEs based on POD model reduction *Automatica* **47** 418–26

[30] Ou Y., Xu C., Schuster E., Luce T.C., Ferron J.R., Walker M.L. and Humphreys D.A. 2011 Receding-horizon optimal control of the current profile evolution during the ramp-up phase of a tokamak discharge *Control Eng. Pract.* **19** 22–31

[31] Xu C., Ou Y. and Schuster E. 2011 Receding horizon control of the magnetic flux bilinear PDE based on sequential linear quadratic control *7th Int. Congress on Industrial and Applied Mathematics* (*Vancouver*, *18–22 July 2011*)

[32] Gaye O. *et al* 2011 Sliding mode stabilization of the current profile in tokamak plasmas *Proc. 50th IEEE Conf. on Decision and Control* (*Orlando, FL*, *12–15 December 2011*) pp 2638–43 doi: 10.1109/CDC.2011.6160442

[33] Gahlawat A. *et al* 2012 Bootstrap current optimization in tokamaks using sum-of-squares polynomials *Proc. 51st IEEE Conf. on Decision and Control* (*Maui, HI*, *10–13 December 2012*) pp 4359–65 doi: 10.1109/CDC.2012.6426638

[34] Vu N.M.T., Nouailletas R., Lefevre L. and Bremond S. 2013 An IDA-PBC approach for the control of 1D plasma profile in tokamaks *Proc. 52nd IEEE Conf. on Decision and Control* (*Florence, Italy*, *10–13 December 2013*) pp 4176–81 doi: 10.1109/CDC.2013.6760530

[35] Argomedo F. *et al* 2013 Lyapunov-based distributed control of the safety-factor profile in a tokamak plasma *Nucl. Fusion* **53** 033005

[36] Barton J.E. *et al* 2012 First-principles model-based closed-loop control of the current profile dynamic evolution on DIII-D *Proc. 24th Int. Conf. on Fusion Energy* (*San Diego, CA*, *8–12 October 2012*) EX/P2–09 www-naweb.iaea.org/napc/physics/FEC/FEC2012/papers/293 EXP209.pdf

[37] Barton J.E. *et al* 2012 Toroidal current profile control during low confinement mode plasma discharges in DIII-D via first-principles-driven model-based robust control synthesis *Nucl. Fusion* **52** 123018
[38] Boyer M.D. *et al* 2013 First-principles-driven model-based current profile control for the DIII-D tokamak via LQI optimal control *Plasma Phys. Control. Fusion* **55** 105007
[39] Boyer M.D. *et al* 2014 Backstepping control of the toroidal plasma current profile in the DIII-D tokamak *IEEE Trans. Control Syst. Technol.* **22** 1725–39
[40] Hinton F. and Hazeltine R. 1976 Theory of plasma transport in toroidal confinement systems *Rev. Mod. Phys.* **48** 239–308
[41] ITER Physics Basis Editors and others 1999 *Nucl. Fusion* **39** 2137
[42] Goldston R.J. 1984 *Plasma Phys. Control. Fusion* **26** 87
[43] Luce T.C. *et al* 1999 Generation of localized noninductive current by electron cyclotron waves on the DIII-D tokamak *Phys. Rev. Lett.* **83** 4550
[44] Politzer P.A. and Porter G.D. 1990 Power threshold for neutral beam current drive *Nucl. Fusion* **30** 1605
[45] Sauter O. *et al* 1999 Neoclassical conductivity and bootstrap current formulas for general axisymmetric equilibria and arbitrary collisionality regime *Phys. Plasmas* **6** 2834
[46] Sauter O. *et al* 1999 Erratum: neoclassical conductivity and bootstrap current formulas for general axisymmetric equilibria and arbitrary collisionality regime *Phys. Plasmas* **6** 2834
Sauter O. *et al* 2002 Erratum: neoclassical conductivity and bootstrap current formulas for general axisymmetric equilibria and arbitrary collisionality regime *Phys. Plasmas* **9** 5140
[47] Martin Y. *et al* 2008 Power requirements for accessing the H-mode in ITER *J. Phys.: Conf. Ser.* **123** 012033
[48] Righi E. *et al* 1999 Isotope scaling of the H-mode power threshold on JET *Nucl. Fusion* **39** 309
[49] Greenwald M. *et al* 1988 A new look at density limits in tokamaks *Nucl. Fusion* **28** 2199
[50] Teo K. *et al* 1991 *A Unified Computational Approach to Optimal Control Problems* (New York: Wiley)
[51] Ferron J. *et al* 1998 Real time equilibrium reconstruction for tokamak discharge control *Nucl. Fusion* **38** 1055–66
[52] Skogestad S. and Postlethwaite I. 2005 *Multivariable Feedback Control Analysis and Design* (New York: Wiley)
[53] Barton J.E. *et al* 2014 Experimental and simulation testing of physics-model-based safety factor profile and internal energy feedback controllers in DIII-D advanced tokamak scenarios *Proc. 19th IFAC World Congress* (*Cape Town*, *25–29 August 2014*) pp 5223–8 doi: 10.3182/20140824-6-ZA-1003.01718
[54] Barton J.E. 2015 Physics-model-based optimization and feedback control of the current profile dynamics in fusion tokamak reactors *PhD Thesis* Lehigh University
[55] Zaccarian L. and Teel A.R. 2011 *Anti-windup Synthesis: Control Augmentation for Actuator Saturation* (Princeton, NJ: Princeton University)
[56] Ferron J. *et al* 2011 Optimization of the safety factor profile for high noninductive current fraction discharges in DIII-D *Nucl. Fusion* **51** 063026
[57] Barton J.E., Wehner W.P., Schuster E., Luce T.C., Jackson G.L., Ferron J.R., Humphreys D.A. and Hyatt A.W. 2014 Optimization of the current ramp-up phase in DIII-D via physics-model-based control of plasma safety factor profile dynamics *56th Annual Meeting of the APS Division of Plasma Physics* (*New Orleans, LA*, *27–31 October 2014*) http://meetings.aps.org/link/BAPS.2014.DPP.NP8.41
[58] Ilhan Z. *et al* 2014 First-principles-driven model-based optimal control of the current profile in NSTX-U *56th Annual Meeting of the APS Division of Plasma Physics* (*New Orleans, LA*, *27–31 October 2014*) http://meetings.aps.org/link/BAPS.2014.DPP.PP8.51
[59] Barton J.E., Schuster E., Felici F. and Sauter O. 2014 Closed-loop control of the safety factor profile in the TCV tokamak *Proc. 53rd IEEE Conf. on Decision and Control* (*Los Angeles, CA*, *15–17 December 2014*) pp 5660–5 doi: 10.1109/CDC.2014.7040275
[60] Barton J.E., Besseghir K., Lister J. and Schuster E. 2013 Robust control of the safety factor profile and stored energy evolutions in high performance burning plasma scenarios in the ITER tokamak *Proc. 52nd IEEE Conf. on Decision and Control* (*Florence*, *10–13 December 2013*) pp 4194–9
[61] Barton J.E., Wehner W.P., Schuster E., Felici F. and Sauter O. 2015 Simultaneous closed-loop control of the current profile and the electron temperature profile in the TCV tokamak *American Control Conf.* (*Chicago, IL*, *1–3 July 2015*) pp 3316–21 doi: 10.1109/CDC.2013.6760533